TECTONO-METAMORPHIC EVOLUTION OF THE CRETACEOUS KLUANE SCHIST, SOUTHWEST YUKON

Will. F. McKenzie [§] and H. Daniel Gibson

Department of Earth Sciences, Simon Fraser University, Burnaby, BC, Canada

Brendan Dyck

Department of Earth, Environmental and Geographical Sciences, University of British Columbia, Kelowna, BC, Canada

Matthew Steele-MacInnis

Department of Earth and Atmospheric Sciences, University of Alberta, Edmonton, AB, Canada

[§] *Corresponding author e-mail address*: *wmckenzi@sfu.ca*

This is a preprint submitted to EarthArXiv. This manuscript has been submitted for publication in THE CANADIAN JOURNAL OF MINERALOGY AND PETROLOGY. Please note that this manuscript is currently undergoing peer-review and is yet to be formally accepted as a publication. Subsequent versions of this manuscript may have slightly different content. Please feel free to contact any of the authors; we welcome feedback.

Abstract

A wealth of information regarding the Mesozoic evolution of the Northern Canadian and Alaskan Cordillera is held within a series of variably metamorphosed and deformed Jura-Cretaceous basins. Located at the interface between the pericratonic Intermontane and exotic Insular terranes, these basins may prove key to understanding the timing and tectonic style of Insular terrane accretion, a topic of longstanding debate. This study unravels the structural and metamorphic evolution of one of these basins, the Kluane Basin, within southwest Yukon Territory.

The Kluane Schist is the primary assemblage of the Kluane Basin. It consists of metamorphosed and deformed low-Al pelites that were intruded by granodioritic plutons of the Paleocene-Eocene Ruby Range Batholith. The Kluane Schist preserves a complex metamorphic history that includes both regional and contact events. Previous workers have suggested the variable metamorphic character of the Kluane Schist represents a large thermal aureole related to Ruby Range Batholith emplacement. Our work, however, indicates the Kluane Schist can be divided into seven distinct petrologic zones, highlighted by a unique combination of mineral assemblage and structure, that together record a period of regional metamorphism coeval with protracted deformation. Further, we propose the Kluane Schist represents a single lithological package which experienced two distinct phases of deformation, 1) an early greenschist-facies phase that resulted in the development of a bedding-parallel chlorite–muscovite–titanite fabric, preserved by its lowest grade units, and 2) a later amphibolite-facies phase that manifests across higher grade units as the progressive transposition of the earlier chlorite–muscovite fabric into a penetrative biotite-rich schistosity that transitions upgrade into a segregated gneissic fabric comprised of biotite–cordierite and plagioclase–quartz (+/- sillimanite–K-feldspar–melt).

By integrating the results of detailed petrography and petrological modelling, we demonstrate that the Kluane Schist preserves metamorphic conditions that align with other Buchan-Style terranes worldwide. Our data defines a field gradient across the Kluane Schist ranging from 3.0–3.5 kbar at 375–400 °C to 4–4.5 kbar at 700–750 °C. This record of a coupled Buchan-style metamorphic-deformational evolution and tops-to-the WNW to W non-coaxial shear structures are consistent with the override of the thermally mature Yukon-Tanana terrane as the principal driver of Kluane Schist metamorphism, rather than intrusion of the Ruby Range Batholith.

Keywords: *Buchan metamorphism; phase equilibria modelling; North American Cordillera; metamorphic field gradient; Insular terrane accretion; water activity.*

1. Introduction

Within the North American Cordillera, the 3000 km long suture between the more inboard Intermontane terranes and the more outboard and exotic Insular terranes is dotted with numerous Jurassic to Cretaceous (Jura-Cretaceous) aged basins (Fig. 1a; *e.g.,* McClelland *et al.,* 1992, van der Heyden, 1992, Hults *et al.,* 2013, Box *et al.,* 2019). Within western Canada and southern Alaska, these Jura-Cretaceous basins are thought to represent a group of mostly deep-water sediments that once filled a terrane-intervening seaway separating the Insular and Intermontane terranes (McClelland *et al.,* 1992, Gehrels *et al.,* 1992, Monger *et al.,* 1994, Hults *et al.,* 2013, Sigloch & Mihalynuk, 2013, 2017, Box *et al.,* 2019). The metasedimentary units within these basins record a period of mid- to Late Cretaceous deformation and metamorphism associated with the accretion of the Insular terranes to the margin of western North America that included the previously accreted Intermontane terranes (*e.g.,* Hults *et al.,* 2013, Box *et al.,* 2019, Vice *et al.,* 2020, Waldien *et al.,* 2021a). This record of tectonism provides important insight into the nature of this suturing event, which remains contested with regard to its timing and principle tectonic driver (*e.g.,* McClelland *et al.,* 1992, Sigloch & Mihalynuk, 2013, 2017, Monger, 2014, Box *et al.,* 2019).

The Cretaceous Kluane Basin within southwest Yukon represents one of these terrane-intervening basins (Fig. 1a; *e.g.,* Mezger, 1997, Israel *et al.,* 2011a). The Kluane Basin is interpreted to have developed in either a back-arc (*e.g.,* Eisbacher, 1976, Lowey, 1992, Mezger *et al.,* 2001) or forearc setting (McClelland & Saleeby, 1992, Israel *et al.,* 2011a, Canil *et al.,* 2015, Waldien *et al.,* 2021b), and is dominated by a sequence of largely homogenous pelitic schists and migmatites collectively referred to as the Kluane Schist (*e.g.,* Tempelman-Kluit, 1974, Eisbacher, 1976) or Kluane Metamorphic Assemblage (Mezger *et al.,* 2001). Previous work has documented a complex metamorphic history within the Kluane Schist, which includes both regional and contact events (*e.g.,* Erdmer & Mortnsen, 1993, Mezger *et al.,* 2001). However, the temporal and spatial extent of these metamorphic events, along with the geological processes responsible for their development remains debated (Erdmer & Mortnsen, 1993, Mezger *et al.,* 2001, Israel *et al.,* 2011a).

The Kluane Schist preserves mineral assemblages ranging from the lower greenschist to upper amphibolite-facies, which have been suggested to derive either from the juxtaposition of two regionally metamorphosed belts of distinct provenance (Erdmer & Mortnsen, 1993), or to be the product of an extensive thermal overprint reflecting a ~5–6 kilometer-wide contact aureole related to emplacement of the Paleocene-Eocene Ruby Range Batholith (Mezger *et al.,* 2001). In this study we use petrological, structural, and chemical data along with petrological modelling to unravel the relationship between the distinct mineral assemblages preserved across the Kluane

Schist and re-evaluate its tectono-metamorphic history. With these new datasets we also re-examine the potential correlations drawn between the Kluane Basin and other Jura-Cretaceous basins within the southwest Yukon (Fig. 1b).

2. Geological Context

The Kluane Schist is the northernmost of four lithological assemblages that lie along the boundary between Yukon-Tanana terrane (assigned as part of the Intermontane superterrane; Monger *et al.,* 1982, Colpron *et al.,* 2007) and Alexander and Wrangellia of the Insular terranes within southwest Yukon (Fig. 1b; *e.g.,* Mezger *et al.,* 2001, Israel *et al.,* 2011a, b, Israel *et al.,* 2015, Vice *et al.,* 2020). Moving from north to south the other three lithological assemblages include the Late Triassic Bear Creek assemblage, a volcano-sedimentary succession with affinity to the Alexander or Taku terranes (Israel *et al.,* 2015) and two Jura-Cretaceous basinal assemblages; the Late Jurassic Dezadeash Formation, derived primarily from the outboard Insular terranes (*e.g.,* Lowey, 2018) and the Early Cretaceous Blanchard River assemblage, which crops out along the southern edge of the Kluane Schist and is considered to be largely derived from the inboard Intermontane terranes (Fig. 1b; Vice, 2017, Vice *et al.,* 2020). To the southeast, the Shakwak fault, an inferred structural feature of unknown kinematics, separates the Kluane Schist from rocks of the Bear Creek assemblage and Dezadeash Formation (Fig. 1b; *e.g.,* Mezger, 1997, Colpron & Nelson, 2011, Israel *et al.,* 2015). To the southwest the Kluane Schist is truncated by the Denali Fault, separating it from rocks of the Insular terranes (Fig. 1b). The northern and eastern contact of the Kluane Schist with overlying Yukon-Tanana terrane rocks is obscured by the intrusion of the extensive Paleocene-Eocene Ruby Range Batholith, a composite plutonic body grading from moderately foliated quartz-diorites at its base to massive quartz-feldspar porphyry up-section (Fig. 1b; Israel *et al.,* 2011a, b).

The Kluane Schist is exposed as a 160 km long, largely northwest-striking belt of graphitic mica-quartz schist and cordierite bearing paragneiss (Fig. 1b; *e.g.,* Mezger *et al.,* 2001, Israel *et al.,* 2011a, b). Metamorphic grade increases away from the core of the Kluane Basin, where the Kluane Schist is characterised by a graphitic muscovite-rich schist, towards its northern and eastern edges where the Kluane Schist becomes increasingly gneissic and locally migmatic, preserving centimetre-scale banding defined by darker layers of biotite–cordierite and lighter layers of quartz–feldspar (Figs. 2 and 3; Mezger *et al.,* 2001, Israel *et al.,* 2011a). Previous petrological modelling has suggested this metamorphic character is the result two distinct metamorphic episodes (Mezger *et al.,* 2001): (1) an initial medium-T, medium-P event (peak; ~7 kbar, 510ºC) that developed mineral assemblages up to garnet-grade synchronous with deformation and (2) a high-T, low-P event (~3.5–4.5 kbar, 530–720ºC) evidenced by the static growth of a staurolite–aluminium-silicate–cordierite sequence within higher-grade amphibolite facies schists and gneisses (Mezger *et al.,* 2001). Mapped isograds relating to this second event run-parallel to, and document an increase in metamorphic grade towards, the Ruby Range Batholith (see Fig. 2 in Mezger *et al.,* 2001). Together with evidence for the annealing of previously developed microstructure, this second event has been suggested to document an extensive, 5–6 km wide contact aureole to the Ruby Range Batholith (Erdmer, 1991, Mezger *et al.,* 2001). Recent studies, however, have reported more complex structural relationships between the highest-grade units of the Kluane Schist (*e.g.,* Israel *et al.,* 2011a) with moderate to strong deformational fabrics preserved at the base of the Ruby Range Batholith suggesting it was initially emplaced syn-tectonically, rather than as a static intrusion (Murphy *et al.,* 2009, Israel *et al.,* 2011a, b).

The age of the Kluane Schist is poorly constrained. Current estimates based on two detrital zircon samples suggest a Late Cretaceous (*ca.* 94 Ma) maximum depositional age (MDA) for the Kluane Schist protolith (Israel *et al.,* 2011a). The age of metamorphism for the Kluane Schist was constrained using the same detrital zircon suite indicating there were at least two significant metamorphic events at *ca.* 82 and 70 Ma (Israel *et al.,* 2011a, Stanley, 2012). Zircon dated from a single dike which crosscuts Kluane Schist foliation constrains major fabric development prior to *ca.* 72–68 Ma (Mezger *et al.,* 2001, Israel *et al.,* 2011a). However, monazite within the same dike provides a significantly younger age of 55.6 ± 0.6 Ma (Israel *et al.,* 2011a), suggesting the dated zircon were potentially inherited from the Kluane Schist host rock.

Other units of the Kluane Basin include volumetrically minor and discontinuous bodies of ultramafic talc-schists that are interleaved with Kluane Schist metasediments ("um" in Figs. 1b and 2). The origin of these ultramafic bodies is contentious; they are either interpreted as dismembered fragments of oceanic crust (Mezger, 2000) or imbricated parts of deep-seated arc-related cumulates exhumed into the Kluane Schist along shear zones in northwest Stikinia presently found ~270 km to the southeast (Canil *et al.,* 2015). Rare, foliated and metamorphosed carbonate bodies have been interpreted to represent olistoliths of Yukon-Tanana terrane affinity ("carbonate" in Fig. 2; Stanley, 2012). However, a detailed provenance analysis is yet to be completed. Hornblende normative diorite to quartz diorite intrusions of the Eocene Hayden Lake Suite are the youngest lithology within the Kluane Basin (*e.g.,* Isreal *et al.,* 2011a, b, Stanley, 2012). These kilometer-scale intrusions are massive and largely undeformed ("Eh" in Fig. 2; Israel *et al.,* 2011b).

Within the southwest Yukon the Blanchard River assemblage (Fig. 1b) represents a similar belt of Jura-Cretaceous metapelitic rocks to the Kluane Schist, with both units suggested to share a similar metamorphic evolution (Mezger *et al.,* 2001, Vice *et al.,* 2020). However, despite their proximal location (Fig. 1b) and similar lithology these units consistently show discrepancy in their preserved mineral assemblage and structure (Mezger *et al.,* 2001, Vice *et al.,* 2020). The Blanchard River assemblage documents similar high-pressure conditions (~6.5 kbar, 635–650ºC) to that suggested for the Kluane Schist (see above; Mezger *et al.,* 2001, Vice *et al.,* 2020), although its mineral assemblages typically contain kyanite (Vice *et al.,* 2020) while its lower-pressure assemblages (~3 kbar) are considered syn-deformational and are clearly shown to overprint previous higher-pressure metamorphism (Vice *et al.,* 2020). Such high-pressure phases (*i.e.,* kyanite) and the distinct syn-deformational overprinting relationships seen across the Blanchard River assemblage have not previously been reported across the Kluane Schist (*cf.* Mezger *et al.,* 2001 & Vice *et al.,* 2020). Equally, within the Blanchard River assemblage the thermal effect of the Ruby Range Batholith is observed as a third, distinct metamorphic event that is restricted to the assemblages directly adjacent to the igneous contact (Vice *et al.,* 2020). These inconsistencies further highlight the need to re-evaluate the metamorphic evolution of the Kluane Schist in order to assess a potential correlation between the two units.

3. Methods

3.1. Analytical methods

3.1.1. Whole rock and mineral chemistry

Six samples were analysed by X-Ray fluorescence spectroscopy (XRF) to determine the variability in bulk composition across the Kluane Schist. XRF analysis was completed by Bureau

Veritas Commodities Canada Ltd, in Vancouver, British Columbia and included eleven major oxides (SiO_2, Al_2O_3, TiO_2, Fe_2O_3, MgO, CaO, MnO, Na_2O, K_2O, P_2O_5 and Cr_2O_3) along with seven trace elements (Ba, Ni, Sr, Zr, Y, Nb, Sc). Selected samples come from a variety of localities and metamorphic grades across the Kluane Schist (red stars, Fig. 2). All bulk rock compositional data can be found in the supplemental table S1.

Mineral chemical analyses were completed on six samples across the Kluane Schist (green stars, Fig. 2) using wavelength-dispersive X-ray spectroscopy (WDS) on a CAMECA SX-5 Field Emission Electron Probe Micro-Analyser (EPMA) at the University British Columbia, Okanagan. We analysed seven major assemblage minerals (chlorite, muscovite, biotite, garnet, staurolite, plagioclase and cordierite). The standards used for calibration were garnet spessartine for Si and Mn, titanite for Ti, garnet almandine for Al and Fe, wollastonite for Ca, albite for Na, diopside for Mg, orthoclase for K, apatite for P, fluorite for F and synthetic KCl for Cl. WDS quantification of Si, Al and F used the LTAP crystal; Ti, Ca, K, P and Cl used the LPET crystal; Fe and Mn used the LLIF crystal; and Na and Mg used the TAP crystal. A 20 keV acceleration voltage and 20 nA beam current was used to maximize analytical resolution and minimize sample damage. We analysed several spot locations across each porphyroblastic phase (garnet, staurolite, plagioclase, cordierite, and coarse biotite) to assess any chemical variations within individual grain. All mineral compositional data can be found in the supplemental tables S2–S8.

3.1.2. Raman spectroscopy

To quantify evolution of water activity (aH_2O) during metamorphism we conducted petrographic and Raman spectroscopic analysis of fluid and graphite inclusions in garnet within sample 19WM118 (118 in Fig. 2). A doubly polished thin section was used for analysis.

Petrography of inclusions was done using an Olympus BX53 microscope and a 100x long working distance objective lens. Raman spectroscopy was done using a Horiba LabRam HR Evolution Raman microscope at the University of Alberta. For Raman excitation, we used a 532 nm (green) laser focused through a 100x long working distance objective and using a confocal pinhole aperture of 50 µm. A grating of 1800 grooves/mm was utilized for high spectral resolution. The nominal laser power was 100 mW at the source, but a neutral density filter in the incident beam path was applied to reduce the power to 25 %. This was to avoid laser damage to the host garnet. Raman spectra were collected using 3 accumulations of 30 s each over the spectral range from 1000 to 4000 cm^{-1} to encompass the Raman bands of CO_2, graphite and H_2O (Frezzotti *et al.,* 2012).

The density of CO_2 in fluid inclusions was estimated by applying a modified version of the Raman CO_2 densimeter of Lamadrid *et al.* (2017). Specifically, Lamadrid *et al.* (2017) showed that the densimeter calibration needs to be adapted to each laboratory by analysis of suitable standards; our analyses used synthetic H_2O-CO_2 fluid inclusions to adjust the calibration curve accordingly. For density calculations, the software package PeakFit was used to extract the peak positions of the CO_2 Fermi diad, using a Gaussian-Lorentzian peak shape and a linear baseline. Bulk composition, density and isochore of the fluid inclusions were estimated using the approach and equations outlined by Steele-MacInnis (2018).

Temperature was estimated based on the crystallinity of graphite mineral inclusions within garnet of sample 19WM118 according to the calibration equation of Beyssac *et al.* (2002). Again, Raman peaks for the D- and G-bands of carbonaceous inclusions were fitted quantitatively using the PeakFit software, Gaussian-Lorentzian peak shapes and a linear baseline (Fig. S1).

3.2. Forward petrological modelling

All phase diagrams were calculated using the petrological modelling software Theriak-Domino (de Capitani & Brown, 1987, de Capitani & Petrakakis, 2010). Modelling was completed within the chemical system MnNCKFMASTHO (MnO–Na_2O–CaO–K_2O–FeO–MgO–Al_2O_2–SiO_2–H_2O–TiO_2–O_2). We tested three combinations of datasets and activity-composition models: (1) ds6.2 of Holland & Powell (2011) coupled with the metapelite HPx-eos of White *et al.,* (2014), (2) the modified SPaC14 dataset of Spear & Cheney (1989) and activity models as described in Pattison & Debuhr (2015) and (3) ds5.5 of Holland & Powell (1998), with activity models for plagioclase (Holland & Powell, 2003, ternary feldspar, Cbar 1 field); biotite, garnet and melt, (White *et al.* 2007); white mica (Coggon & Holland 2002; margarite omitted); ilmenite (White *et al.* 2000); orthopyroxene, (White *et al.* 2002); and staurolite, chlorite, cordierite and H_2O, (Holland & Powell 1998). Clinozoisite and zoisite are modelled as pure end-member phases within our ferric-free chemical system.

Of these three modelling combinations none fully satisfies all our observed natural mineral relationships across the Kluane Schist (Figs. S2–4). In particular, the cordierite-free andalusite–biotite–garnet +/- muscovite (+ plagioclase–quartz) assemblage (assemblage 5a in Fig. 2) is not produced by any modelling combination. Potential reasons and solutions to this are discussed in detail in section 5. Aside from the absence of assemblage 5a, models run with ds5.5 provide a better prediction of our observed mineral assemblages, and importantly, the order of observed paragenesis across the Kluane Schist than either ds6.2 or SpaC14 (*cf.* Figs. S2–4). Models run with the more recent ds6.2 do not produce the biotite-free, zoisite-bearing assemblages observed within the lower-grade units of the Kluane Schist (assemblage 2a in Figs. 2 and S4) or the sillimanite-free cordierite bearing assemblages typical of higher-grade units (assemblage 6b in Figs. 2 and S4). Models run with the SPaC14 dataset predict zoisite-bearing mineral assemblages down temperature of chlorite–muscovite–titanite, the opposite to that observed across the Kluane Schist (Figs. 2, 3 and S3) while the occurrence of garnet downgrade of staurolite is predicted at significantly higher pressures than that suggested by either ds5.5 or ds6.2 (Figs. S2–4). Models run with the SPaC14 dataset also fail to produce the sillimanite-free cordierite bearing assemblages typical of the higher-grade units of the Kluane Schist (assemblage 6b in Figs. 2 and S3). As such we choose ds5.5 for our final models. Recent studies have highlighted similar results when comparing modelling results to observed metapelitic assemblages (*e.g.,* Waters, 2019, Dyck *et al.,* 2020), especially when considering a ferric-free system and cordierite-bearing equilibria (Pattison & Goldsmith, 2022).

Additionally, we incorporate the results from garnet fluid inclusion analysis to produce a phase diagram that accounts for variable $a$$H_2O$ with metamorphic grade. This is discussed in detail in section 5. Finally, our model considers excess free H_2O at sub-solidus conditions and only the amount of H_2O required to minimally saturate the assemblage in the immediate sub-solidus in the supra-solidus domain (*cf.* Dyck *et al.,* 2020, Pattison & Goldsmith, 2022). In order to account for the decrease in melt H_2O content with decreased pressure (*e.g.,* Brown *et al.,* 1995) we also separate out the supra-solidus domain into two regions (1.5–3.5 kbar and 3.5–5.5 kbar), with each modelled independently with its associated minimally saturated H_2O composition (2.7 mol H_2O at 2 kbar for the 1.5–3.5 kbar domain and 3.0 mol H_2O at 4 kbar for the 3.5–5.5 kbar domain; *cf.* Pattison & Goldsmith, 2022; T-XH_2O diagrams in Fig. S5). Our resulting phase diagram stiches these supra- and sub-solidus regions at their common wet solidus.

3.3. Thermobarometry

To complement our forward petrological modelling and provide further constraint on the metamorphic conditions experienced by the Kluane Schist, we calculated the peak conditions experienced by four samples across the Kluane Schist using thermobarometry (19WM262, 19WM120, 19WM118, 19WM123; sample locations on Fig. 2). Peak pressure conditions were estimated by applying multi-equilibria thermobarometry using the AvP function within the *Thermocalc* software package (version tc345 with ds5.5, Holland & Powell, 1994). Mineral end-member activities were calculated using *AX* (Holland & Powell, 2009) to remain consistent with our chosen activity models for forward petrological modelling. A particular advantage to this approach is the ability to define $a\mathrm{H_2O}$ for calculation which has been shown to greatly improve the accuracy of results (*e.g.,* Holland & Powell, 2008, Waters, 2019). As such, AvP calculations were completed with $a\mathrm{H_2O}$ values in line with the results from our Ramen spectroscopy, graphite crystallinity and constraints provided by our forward phase equilibrium modelling.

Conventional barometry calculations were completed using the garnet–muscovite–biotite–plagioclase barometer (Wu, 2015) and the garnet–biotite–aluminium-silicate–quartz barometer (Wu, 2017). For graphite-free samples temperatures were also calculated using the garnet-biotite thermometer (Holdaway, 2000). Conventional thermometry was not applied to graphite-bearing samples due to the large imprecision in thermometer equilibria when $a\mathrm{H_2O}$ cannot be assumed = 1 (*e.g.,* Waters, 2019). Across all conventional thermobarometry calculations we set $X\mathrm{Fe}^{3+}$ = $\mathrm{Fe}^{3+}/\mathrm{Fe}_{\mathrm{total}}$ as 0.11 for biotite (*e.g.,* Forshaw & Pattinson, 2021), and assumed a negligible Fe^{3+} component to garnet (*e.g.,* Dyar *et al.,* 2002, Forshaw & Pattinson, 2021).

4. Results

4.1. Petrology and field relationships across the Kluane Schist

The overall structure of the Kluane Schist is dominated by a largely northwest striking, northeast dipping schistosity which shows limited variation across its current exposure (Figs. 1b and 2). Within the central region of the basin this schistosity can be observed to locally dip south, defining an antiform that plunges shallowly towards the east and deflects mineral isograds (Fig. 2; *cf.* Mezger *et al.,* 2001). Combined with the general increase in metamorphic grade moving from its core towards the north and east (Fig. 2), the Kluane Schist defines an inverted, hot-side-up metamorphic field gradient towards its contact with the Ruby Range Batholith (Fig. 2; *e.g.,* Muller, 1967, Erdmer & Mortnsen, 1993, Mezger *et al.,* 2001, Israel *et al.,* 2011a, b). A normal metamorphic field gradient is also observed to reach at least staurolite-grade along the southeastern edge of Kluane Lake (Figs. 2 and 3). The distribution of mineral assemblages recorded in this and previous studies (Mezger *et al.,* 2001) potentially reflects an extension of the overturned southern limb of the east plunging antiform observed to the west (Fig. 2). Combined, our detailed petrography and fieldwork, using over 300 field localities and 65 thin sections, suggests that the evolution of major structures observed across the Kluane Schist is intrinsically linked to the mineral assemblages preserved. As such, we divide the Kluane Schist into seven unique petrological zones which consist of units with a distinct combination of mineral assemblage, microstructure and outcrop style (Figs. 2 and 3).

4.1.1. Fabrics preserved in the Kluane Schist

The structures observed across the petrologic zones within the Kluane Schist are consistent with two distinct phases of deformation (Figs. 2–4). The first of these, D_1, is best preserved within the lowest-grade units of the Kluane Schist in the form of a bedding parallel chlorite–muscovite–titanite–calcite foliation, S_1 (Figs. 3i and 5a-b). Striking west and dipping moderately to the north, S_1 is the lowest-grade fabric observed across the Kluane Schist (Fig. 3a). To north and south, this foliation is progressively transposed by a second phase of deformation, D_2, into a penetrative, regional S_2 foliation (Figs. 2 and 3a). The progressive transposition of S_1 is recorded across the Kluane Schist by: 1) initial crenulation of S_1 to form an oblique S_{2a} fabric that commonly defines an axial planar cleavage to symmetrical F_{2a} folds (Figs. 3h, and 5b), and 2) the progressive reorientation of S_{2a} into a pervasive WNW-striking, NNE-dipping biotite-rich foliation, S_{2b} (Fig. 3f). S_{2b} can often be seen accompanied by symmetrical, rootless and isoclinal F_{2b} folds (Fig. 3f). Within the highest-grade units of the Kluane Schist, biotite-rich S_{2b} folia are progressively coarsened and segregated to form a cm-scale gneissic banding (Fig. 3b).

$D_{1\text{-}2}$ generally records a period of coaxial flattening deformation dominated by S-tectonites defined by $S_{1\text{-}2a}$ fabrics and planar S_{2b} folia (Figs. 3 and 4). At low metamorphic grade, units show symmetric pinch and swell structures (Fig. 3i), while medium-grade units show symmetric F_{2a} and F_{2b} folds (Fig. 3f, h) along with the symmetrical wrapping of the matrix around porphyroblasts of index minerals that contain straight inclusion trails (Fig. 3g). These observations all imply the predominance of pure shear and flattening during early Kluane Schist deformation (*e.g.,* Spry, 1974, Law, 1986, Mukherjee, 2017). At higher metamorphic grades poikiloblasts exhibit rotated inclusion trails and are commonly asymmetrically wrapped by the matrix foliation (Fig. 3e). This is attributed to a greater influence of simple shear during higher-grade metamorphism and later-stage Kluane Schist deformation (Figs. 3 and 4; *e.g.,* Zwart, 1962, Brown *et al.,* 1995, Mezger, 2010). In general, our observations consistently document greenschist- to granulite-facies metamorphism coeval with evolving deformation (Figs. 3 and 4). This contrasts previous hypotheses that suggest these mineral assemblages were developed statically in response to the intrusion of the Ruby Range Batholith (Erdmer, 1991, Mezger *et al.,* 2001). We do not refute evidence for static fabric overgrowth within the Kluane Schist (*e.g.,* Figs. 3c and 4), however, these microstructures are largely confined to its structurally highest units nearest the contact with the Ruby Range Batholith (Fig. 3). Further, static overprinting of regional high-grade assemblages need not occur within a contact aureole. This is an observation commonly recorded across regionally metamorphosed orogenic belts (*e.g.,* Cashman & Ferry, 1988, Moller & Sonderlund, 1997, Gibson *et al.,* 2005) where post-deformational annealing and coarsening of stable mineral assemblages has been attributed to the dissipation of accumulated lattice strain energy during steady thermal relaxation (*e.g.,* England & Thompson, 1984, Hickey & Bell, 1996, Gibson *et al.,* 2005). Notwithstanding, our field and petrographic observations are most consistent with a coupled tectono-metamorphic history for the Kluane Schist where an increase in metamorphic grade is mirrored by the intensity of ductile deformation (Figs. 3 and 4).

4.1.2. Petrological Zones of the Kluane Schist

Zone 1: chlorite–muscovite schist. The lowest grade units of the Kluane Schist are found at its structurally lowest levels (Fig. 3). Zone 1 units are lustrous and silver-blue in appearance (Fig. 5a insert). Compositional banding (S_0) is readily observed in outcrop and defined by distinct carbonaceous, quartz-rich and mica-rich layers (Fig. 5a). The more aluminous mica-rich domains contain plagioclase porphyroblasts along with muscovite and chlorite (Fig. 5a insert). Millimetre-scale quartz banding is often seen parallel to compositional banding.

Zone 1 schists consist of a mineral assemblage containing chlorite–muscovite–plagioclase–quartz +/- titanite–calcite (Fig. 5b). Muscovite–chlorite–titanite–calcite defines S_1, which is overgrown by plagioclase with inclusions of titanite, quartz, chlorite, muscovite, and graphite (Fig. 5b). S_1 fabrics are locally crenulated into a muscovite-rich S_{2a} (Fig. 5b). Plagioclase is wrapped by S_{2a} and often preserves inclusion trails oblique to both S_1 and S_{2a} (Fig. 5b). Cm-scale, close to tight F_{2a} folds are locally observed within outcrop. S_1 foliations are more strongly crenulated within the hinge zones of these F_{2a} folds (Fig. 3h).

Zone 2: biotite-zoisite schist. Moving away from the core of the Kluane Schist, metamorphic grade increases with structural level (Figs. 2 and 3). Zone 2 rocks are a darker blue colour and less lustrous than in zone 1 (Fig. 3h). Quartz bands appear coarser and locally recrystallised (Fig. 3h). S_0 is difficult to make out in outcrop due to a more pervasive overprinting by tight and reclined F_{2a} folds (Fig. 3h). S_1 represents the dominant planar fabric within zone 2 and is defined by an assemblage of chlorite–muscovite–quartz–plagioclase–graphite +/- ilmenite–biotite–zoisite (Fig. 5 c, d). The assemblage of zone 2 lacks titanite and shows a reduction in calcite abundance compared with zone 1 (Fig. 5 c, d). Muscovite shows an increased abundance in zone 2 while chlorite abundance is reduced compared with zone 1 (Figs. 5c, d). S_{2a} fabrics are strongly developed within F_{2a} fold hinges and comprise biotite–zoisite–muscovite–ilmenite–graphite +/- chlorite–hematite (Fig. 5d). Graphite is more abundant in zoisite bearing lithologies. Biotite is seen upgrade of zoisite and is associated with the strong development of S_{2a} fabrics (Fig. 5d). Biotite abundance steadily increases moving upgrade across zone 2, while chlorite and muscovite decrease in abundance. S_{2a} fabrics are strengthened with increased structural level and metamorphic grade and are commonly observed to crosscut chlorite-rich S_1 fabrics within the highest-grade units of zone 2 (Fig. 5d). Plagioclase porphyroblasts preserve rotated S_1 inclusion trails and are wrapped by the S_{2a} fabric (Fig. 5c).

Zone 3: garnet-biotite schist. Continuing up structural section from zone 2, the Kluane Schist is distinctly darker in colour, losing the blue hue common to the lower-grade units (Fig. 6a). All traces of S_0 are lost in zone 3 outcrops (Fig. 6a). Quartz banding is regularly spaced and is parallel to S_{2a} (Fig. 6a). Reclined F_{2a} folds are tightened and often dismembered moving up-section within zone 3 (Figs. 6a). Although these folds are tighter and almost isoclinal in places, F_{2a} can still be readily identified within a given outcrop and their symmetrical geometry can be traced at the metre-scale (Fig. 6a).

The typical mineral assemblage of zone 3 consists of biotite–plagioclase–muscovite–garnet–chlorite–quartz–ilmenite +/- zoisite–calcite (Fig. 6b, c, d). Both garnet and plagioclase host inclusions of zoisite and calcite within the lowest grade regions of zone 3 (Figs. 6b, c and S6). At these lower grades, garnet shows macroscopically rational crystal face development with its radial, hexagonal growth pattern outlined by matrix graphite and inclusions of quartz and zoisite (Fig. 6b). Zoisite is lost from the assemblage a short distance up-grade of the first appearance of garnet (Fig. 6c *versus* 6d). Within these zoisite-free assemblages garnet remains coarse, albeit less euhedral, and is partially wrapped by S_{2a} (Fig. 6d). At these higher grades garnet hosts inclusions of S_1 quartz, biotite, graphite, and calcite (Fig. 6d). Plagioclase is abundant throughout zone 3 assemblages, typically hosting chlorite, graphite and biotite inclusion trails that align with relic S_1 fabrics (Fig. 6d). Plagioclase also commonly has distinctly inclusion free rim domains which show partial wrapping by the S_{2a} fabric (Fig. 6b, d). Chlorite and muscovite show a decreased abundance compared with zones 1 and 2 and are largely restricted to S_1 orientations (Fig. 6d). The more dominant S_{2a} foliation is primarily defined by biotite (Fig. 6d). This microstructural-mineral relationship is progressively reinforced with increased metamorphic grade across zone 3 (Fig. 6b, c, d).

Zone 4: staurolite schist. Structurally above zone 3, the staurolite-bearing mineral assemblages that define zone 4 are observed (Figs. 2 and 3). Rocks of zone 4 are dark in colour and $S_{0\text{-}1}$, S_{2a} and F_{2a} are no longer observed in outcrop (Fig. 3f). Instead, outcrops are dominated by S_{2b} and isoclinal F_{2b} intra-folia folds (Fig. 3f). Quartz banding is penetrative and regularly spaced, paralleling S_{2b} (Fig. 3f).

The assemblage typical of zone 4 rocks consists of staurolite–biotite–muscovite–plagioclase–quartz–ilmenite +/- garnet–chlorite (Fig. 3g). There is a reduced abundance of muscovite and chlorite as compared with zones 1-3. Staurolite and plagioclase form the major porphyroblasts within zone 4. Staurolite exhibits a prismatic habit, elongate parallel to, and wrapped by the biotite S_{2b} foliation (Fig. 3g). Plagioclase porphyroblasts are wrapped by S_{2b} and contain inclusion trails of graphite and biotite that are oblique to S_{2b}. Garnet occurs locally in aluminous domains and has a cloudy appearance due to abundant graphite and fluid inclusions (Fig. 3g). Garnet rims show an embayed texture and are locally infilled by quartz, biotite, muscovite and occasionally plagioclase (Fig. 3g). Garnet is wrapped by S_{2b} fabrics and shows inclusions of quartz and S_{2b}-oriented biotite and graphite (Fig. 3g). This relationship suggests garnet grew syn-kinematically during S_{2b} development.

Zone 5: andalusite/sillimanite schist. Continuing up structural section, outcrops within zone 5 are dark in colour and dominated by a biotite-rich S_{2b} schistosity along with a centimetre-scale penetrative quartz banding (Fig. 3d). This penetrative quartz-rich banding can be seen to have developed through the shearing out of rootless F_{2b} fold limbs into the foliation plane (Fig. 3d). This transposition of F_{2b} folds within zone 5 lithologies marks the initial development of the distinct gneissic banding common to units within zones 6 and 7. Upgrade across zone 5, the occurrence of F_{2b} folds decreases as the Kluane Schist is progressively dominated by a coarse and regularly spaced gneissic band (Fig. 3b, d).

Directly upgrade of zone 4, the rocks of zone 5 consist of the assemblage andalusite–plagioclase–biotite–garnet–ilmenite +/- muscovite–staurolite–sillimanite (Fig. 6e). Andalusite first appears as knotty anhedral porphyroblasts that in are locally intergrown with the S_{2b} fabric and quartz (Fig. 6e). Graphite is largely lost from the matrix of zone 5 lithologies, only observed as inclusions within coarser porphyroblasts (Fig. 6e). Staurolite occurs as relic porphyroblasts within zone 5 with their direct replacement by andalusite evidenced by local staurolite relics remaining preserved as inclusions within andalusite poikiloblasts (Figs. 3e and 6e). Andalusite poikiloblasts also host biotite, muscovite, and quartz inclusions (Figs. 3e and 6e). Most andalusite grains are wrapped by S_{2b} fabrics and appear elongate and aligned with S_{2b}. In some domains andalusite has curved biotite inclusions trails, suggesting it grew syn-kinematically during clockwise non-coaxial shear (Fig. 3e). Prismatic plagioclase also shows elongation parallel to the S_{2b} fabric within zone 5 (Fig. 6f). Plagioclase cores host a variety of inclusion orientations like that seen in zone 4. In contrast, the tips of prismatic plagioclase are distinctly graphite free and locally show inclusions of fine biotite, andalusite and fibrolitic sillimanite with S_{2b} orientations (Fig. 6f). Garnet is also observed within zone 5 assemblages. Garnet is euhedral and shows distinctly inclusion-free outer domains, mantled on the cloudy, fluid inclusion-rich cores common to zone 4 (Fig. 7c). Finer, inclusion-free garnet is also observed included within graphite free plagioclase domains (Fig. 6f). Muscovite is less abundant compared with zone 4, and is observed within S_{2b} fabrics and included within andalusite porphyroblasts (Figs. 3e and 6e).

Higher-grade units within zone 5 show an increased abundance of fibrolitic sillimanite where it generally occurs associated with biotite-rich S_{2b} fabrics (Fig. 6f). The abundance of fibrolitic sillimanite within zone 5 assemblages coincides with the replacement of relic andalusite porphyroblasts with muscovite and the growth of prismatic plagioclase tips (Fig. 6f, insert). Locally within higher grade regions of zone 5, prismatic sillimanite occurs along with fibrolitic sillimanite (Figs. 2 and 7a). Andalusite and staurolite are absent from these units. Prismatic sillimanite occurs parallel to S_{2b}, wrapping both garnet and plagioclase (Fig. 7a). Within these units, clear inclusion-poor garnet porphyroblasts are wrapped by S_{2b} fabrics. Garnet cores host inclusion of quartz, biotite and rare graphite that run oblique to the S_{2b} fabric, while garnet rims are distinct and inclusion-free (Fig. 7a).

Zone 6: cordierite gneiss. Farther up structural section, zone 6 outcrops are dominated by a coarse, centimetre-scale penetrative gneissic banding and often take on a faint orange colour (Fig. 3b). Cordierite abundance increases rapidly within zone 6, occurring primarily within darker, biotite-rich bands, while lighter bands consist of quartz and plagioclase (Fig. 7c). This change in minerology and structure has led previous workers to suggest these gneissic units may be of different affinity to the Kluane Schist (Erdmer, 1991, Mortensen and Erdmer, 1993, Israel *et al.,* 2011a, b). However, rare relic F_{2b} folds can be found that, although are typically dismembered, show a similar geometry to those downgrade (Fig. 3a, b). Within the highest-grade regions of zone

6, gneissic banding remains penetrative, but is coarser and the contrast between light and dark bands is undulous and irregular (Fig. 3b).

Just upgrade from zone 5, zone 6 lithologies consist of an assemblage including cordierite–biotite–quartz–plagioclase–muscovite–ilmenite +/- garnet–andalusite–sillimanite–staurolite (Fig. 7b). Abundant elongate cordierite is associated with the biotite–muscovite S_{2b} fabric and can be seen wrapping local poikilioblasts of andalusite and staurolite, which show limited evidence of corrosion (Fig. 7b). Andalusite poikilioblasts generally lack the muscovite inclusions observed within zone 5 (Fig. 7b). Upgrade within zone 6 prograde muscovite is also lost from the S_{2b} fabric (Fig. 7c). The euhedral, graphite free garnet crystals typical of zone 5 also show strong corrosion and embayment by cordierite within these higher-grade gneisses (Fig. 7c). Fibrolitic sillimanite occurs towards the base of zone 6 and shows a general decrease in abundance moving structurally upward with a corresponding increase in cordierite (Figs. 7b *versus* 7c *versus* 3c). The majority of plagioclase porphyroblasts show alignment with the S_{2b} fabric and host inclusions of biotite, quartz, and graphite, but never cordierite (Fig. 7c). Instead, cordierite can be seen to wrap both plagioclase and garnet (Fig. 7c). Within the highest-grade units of zone 6, cordierite is coarse and euhedral, often overgrowing bundles of fibrolitic sillimanite and S_{2b} fabrics (Fig. 3c). Fibrolitic sillimanite-free biotite shows coarsening and growth semi-oblique to the S_{2b} fabric and local garnet shows atolls of biotite and cordierite (Fig. 3c). Both cordierite and biotite retain a general orientation sub-parallel with S_{2b} fabrics (Fig. 3c).

Zone 7: migmatite. Polymineralic plagioclase–quartz–cordierite leucosome appears to be locally developed within isolated northern regions of the Kluane Schist (Figs. 2 and 7f). Plagioclase and cordierite are euhedral and equant, and do not have a particular shape preferred orientation (Fig. 7f). Quartz is coarse and irregular in shape showing undulous extinction and apparent quartz–plagioclase–plagioclase dihedral angles <45° (Fig. 7f). Spongy and randomly orientated muscovite and chlorite are interpreted as retrograde phases (Fig. 7f). Towards the southern edge of zone 7 (Figs. 2 and 3) stromatic migmatites occur (Fig. 7d), while towards the north and in contact with the Ruby Range Batholith zone 7 contains schollen-style migmatites (Mehnert, 1968). Locally, in areas which have undergone foliation collapse or folding, leucosome within stromatic migmatites can take on a star or web appearance (Fig. 7d). Consistent tops-to-the-SSW orientation among these structures suggests melt migration into several sinistral shear bands (Fig. 7d; *e.g.,* Brown *et al.,* 1995).

Paleosomes within zone 7 are typically a faint orange colour and consists of quartz–biotite–cordierite–plagioclase +/- K-feldspar–garnet–fibrolite (Fig. 7d, e). A regularly spaced, centimetre-scale gneissic banding is present and is similar to that observed within zone 6 (Fig. 7d, e). F_{2b} folding is not readily observed within outcrop. Rare, corroded staurolite are present and preserve aligned graphite inclusion trails like those seen in zone 4 (Fig. 7e). Garnet is anhedral and corroded, preserving atolls of muscovite, chlorite and cordierite. Fibrolitic sillimanite shows a marked decrease in abundance, only locally occurring as inclusions within coarse cordierite (Fig. 7e). Local K-feldspar is associated with biotite-rich domains and appears to overgrow biotite S_{2b} fabrics (Fig. 7e). Cordierite shows two distinct populations within migmatic units; one roughly aligned with S_{2b} fabrics, which hosts sillimanite inclusions (crd$_{(1)}$) and a second which shows an irregular shape, overgrows S_{2b} and lacks sillimanite inclusions (crd$_{(2)}$; Fig. 7e).

4.1.3. Late deformation features

The rocks of the Kluane Basin experienced two additional deformation events prior to final exhumation (Fig. 4). These events, D_3 and D_4, had a limited effect on the preserved mineral assemblage but act to modify the original orientation of the fabrics and petrologic zones developed during D_2.

D_3 occurred during a period of non-coaxial strain. L-tectonics are developed that preserve a mineral alignment lineation which trends NE–SW. In the sense-of-shear plane viewed parallel to the mineral alignment lineation, asymmetrical shear folds, F_3, verge SSW to SW, and asymmetrical boudinaged quartz pegmatites provide a tops-to-the-SW sense of shear (Fig. 8). Both structures overprint previously developed S_2 fabrics and suggest a period of SSW-to SW- directed shear during D_3 (Fig. 8).

D_4 is associated with the development of open buckle folds that are 10s m to km in wavelength and trend E-W with a moderate plunge in both directions (Fig. 2). These folds overprint all earlier fabrics ($D_{1\text{-}3}$) and are interpreted to have significantly post-dated their development, as suggested by their more brittle nature. D_4 likely led to the development of the east-plunging antiform which is observed to deflect our mapped mineral isograds and petrological zones within the central and southwestern regions of the Kluane Schist (Fig. 2).

4.2. **Whole rock and mineral chemistry**

The range of whole rock compositions from the Kluane Schist are summarised in figure 9a, b. Trends in mineral composition as a function of petrologic zone are shown in figure 9c–h. Figure 9i plots the zonation preserved by representative plagioclase crystals from zones 1 and 3–7. All raw whole rock and mineral chemistry data tables are found in S1-S8.

4.2.1. Whole rock chemistry

Whole rock compositions plot within a tight cluster in AFM space with limited apparent grade-dependent variation (Fig. 9a). Differences in Si, Na and Ca for all samples are accounted for by projection from quartz and feldspar (Fig. 9a). An additional projection from apatite and ilmenite is applied to all whole rock compositions except for 18WM06 ("06" in Fig. 9a), where we project from titanite, rather than ilmenite, based on the observed mineral assemblage (*cf.* Figs. 4 and 5b). Whole rock A' values [molar (Al-3K-Na-2Ca)/2] (Spear, 1993) range from 0.005–0.027, with difference in A' value showing no relation to metamorphic grade (Fig. 9a and Table S1). A' values of the Kluane Schist are typical of low-Al pelites, plotting below the garnet-chlorite tie line in AFM space (Fig. 9a; *e.g.,* Thompson, 1957, Spear, 1993). We also observe a limited variability of 0.36–0.39 in whole rock [Mg/(Mg+Fe)] across the Kluane Schist (Fig. 9b and Table S1). Whole rock [Ca/(Ca+Na)] shows a larger variability between 0.13–0.34, however, when one muscovite schist sample is removed ("06" of zone 1), this difference is reduced to 0.28–0.34 (Fig. 9b and Table S1). The general lack of variation in the whole rock chemistry with changes in the mineral assemblage preserved suggests the distribution of our petrological zones across the Kluane Schist is not primarily controlled by bulk composition (*cf.* Fig. 2).

4.2.2. Biotite, chlorite and cordierite

Biotite, chlorite and cordierite largely co-vary with a trend of decreasing Mg/(Mg + Fe) with increasing metamorphic grade between zones 3–7 (Fig. 9c). In contrast, chlorite within zone 1 shows the lowest average Mg/(Mg + Fe) across the Kluane Schist (Fig. 9c). The more widely spread Mg/(Mg + Fe) values obtained from chlorite within zones 6–7 (Fig. 9c) come from a secondary population which overgrows prograde fabrics. Cordierite shows two populations within zone 7 with distinct Mg/(Mg + Fe) values; these correlate with the two cordierite populations observed in thin section (Fig. 9c; *i.e.,* $crd_{(1)}$ and $crd_{(2)}$ in Fig. 7e). Overall, the trends we observe in biotite, chlorite and cordierite Mg/(Mg + Fe) appear independent of whole-rock bulk composition (*cf.* Fig. 9a, b, c). Additionally, biotite shows an increase in Ti across all petrological zones (Fig. 9d) with two distinct populations ($bt_{(1)}$ and $bt_{(2)}$) highlighted by a variation in Si cations between zones 5 and 6 (Fig. 9e)

4.2.3. Muscovite

Muscovite K/(Na + K) varies between 0.76–0.97 showing a decrease from an average of 0.94 in zone 1 to 0.81 in zone 3 (Fig. 9f). Zone 1 muscovite has the highest average K/(Na + K) across the Kluane Schist (Fig. 9f). From zone 3, muscovite K/(Na + K) increases with metamorphic grade from 0.81 in zone 3 to 0.87 in zone 6 where prograde muscovite is lost from the assemblage (Fig. 9f). The Tschermak content of muscovite, measured in this study as Si cations per 22-oxygen formula unit, shows significant spread in zone 1 with values ranging between 5.79–6.74 (average: 6.37; Fig. 9g). Upgrade muscovite shows a more restricted range of Tschermak contents between 5.87–6.13 with no significant variation with grade (Fig. 9g).

4.2.4. Plagioclase

Plagioclase compositions (Xan) range widely across the Kluane Schist (Fig. 9h). There is a significant increase in anorthite content moving between zone 1 and 3; plagioclase from zone 1 is almost entirely albitic (Xan < 0.02) while zones 3–7 exhibit a spread of compositions between oligoclase and andesine (Fig. 9h). This variation shows correlation with an increase in whole rock Xan (*cf.* Fig. 9b). Across zone 3–6 there is a general decrease in Xan and an overall reduction in the range of plagioclase compositions returned from each sample, except for the upper portion of zone 6 near the transition to zone 7 (Fig. 9h). Between zones 6–7 there is a slight increase in plagioclase Xan (Fig. 9h). Plagioclase zonation (in terms of Xan) is limited within zone 1 albite (Fig. 9i). Zone 3 plagioclase typically preserves more anorthite rich cores (Xan ~0.31–0.39) than rims (Xan ~0.26–0.37) (Fig. 9i). Within zones 5 and 6 plagioclase shows more variable zonation patterns with grains showing both normal and reverse zonation to no zonation at all (Fig. 9i). Zone 7 plagioclase generally lacks significant chemical variation (Fig. 9h, i).

4.2.5. Garnet

The Kluane Schist hosts four distinct populations of garnet: (1) coarse, euhedral graphite-rich garnet common to zone 3 assemblages (*e.g.,* Fig. 6c, d); (2) cloudy, embayed and corroded garnet which is rich in fluid inclusions and associated with zone 4 staurolite bearing assemblages (*e.g.,* Fig. 3g); (3) inclusion free garnet which occurs mantled on cloudy garnet cores in zones 5–6 and as individual grains within zone 5 (*e.g.,* Fig. 6f and 7c); and (4) corroded garnet within zones 6–7 which is often embayed by, and shows atolls of cordierite and biotite (*e.g.,* Fig. 3c and 7c). Each of these garnet populations has a unique chemistry outlined below. Full garnet chemical profiles can be found in table S9.

Population (1) garnet cores are characterised by high-grossular (0.20 molar fraction) and spessartine contents (~0.16). In zone 3 both grossular and spessartine then show steady decrease towards zone 3 garnet rims (~0.05, ~0.1, respectively; Table S9). Mg/(Mg + Fe) values generally show a steady increase from ~0.12 within garnet cores to ~0.16 at garnet rims (Table S9). A sharp increase in spessartine and decrease in Mg/(Mg + Fe) is observed within ~140–150 µm of garnet rims (Table S9). The absence of other porphyroblasts within the analysed sample along with garnet preserving a generally euhedral texture (Fig. 6c, d) suggests this zonation pattern largely reflects growth rather than resorption (*e.g.,* Pattison & Tinkham, 2009). The sharp increase in spessartine observed within garnet rims may reflect the consumption of ilmenite during garnet growth (*e.g.,* Pattison & Tinkham, 2009). However, as ilmenite occurs within the matrix and we do not observe the associated Mg-enrichment suggested to accompany ilmenite breakdown, we instead interpret garnet rim chemistry to represent limited resorption (Table S9; *e.g.,* Conolly & Cesare, 1993, Kohn & Spear, 2000, Pattison & Tinkham, 2009)

Compositional profiles across cloudy population (2) garnet are highly variable (Table S9). Population (2) garnet typically preserves spessartine-rich, grossular-poor cores (Table S9). Core to rim Mg/(Mg + Fe) values for population (2) garnets are also highly asymmetrical and show an inconsistent variation between crystals (Table S9). All analysed crystals consistently record a sharp increase in spessartine content towards their rim coupled with a decrease in Mg/(Mg + Fe) that likely reflect a period of garnet resorption (Table S9; *e.g.,* Kohn & Spear, 2000, Pattison & Tinkham, 2009). We interpret this resorption to reflect a period of garnet consumption during the growth of the Mg-rich staurolite that typifies both zone 4 and 5 assemblages across the Kluane Schist (*e.g.,* Fig. 3g and Table S6; Dempster *et al.,* 2017).

Population (3) garnets comprise inclusion free rims that are typically mantled on fluid-rich, cloudy population (2) cores (*e.g.,* Fig. 7c). Population (3) garnet appears in common association with zone 5-6 aluminium silicate bearing assemblages (Fig. 6f). Within these higher-grade assemblages both garnet populations (2 & 3) show more uniform chemical profiles compared with garnet downgrade (Fig. 10 and Table S9). However, we do observe a consistent change in garnet chemistry when traversing from inclusion-rich garnet cores to inclusion-free mantles (Fig. 10). There is a consistent decrease in grossular from 0.06 to 0.04 molar fraction and increase in almandine molar fraction from 0.72 to 0.74, which occurs over a narrow interval (<40 μm) where inclusion-free garnet was analysed adjacent to cloudy garnet (Fig. 10). The smaller, inclusion-free garnet grains within zones 5 and 6 (*e.g.,* Fig. 6f) have similar chemistry to that of inclusion-free regions of larger garnet and are thus assigned to population (3) (dashed lines in Fig. 10). Towards the edge of these inclusion-free domains, within ~80–130 μm of garnet rims, increased spessartine and decreased Mg/(Mg + Fe) likely records a degree of garnet resorption (Fig. 10; Kohn & Spear, 2000, Pattison & Tinkham, 2009). This most likely occurs in response to cordierite growth as suggested by the association of our analysed garnet, cordierite, and sillimanite (Figs. 7c and 10).

Garnet population (4) from zone 7 lacks the systematic variation in chemistry with inclusion pattern as seen in zones 5–6 (Table S9). Uniform grossular and spessartine profiles are seen across all garnets from zone 7 (Table S9). Strong variation in garnet composition in proximity to cordierite atolls suggests exchange of cations and re-equilibration with the surrounding rock matrix was the key driver for the chemical profiles preserved by zone 7 garnet (Table S9).

4.3. Garnet-hosted fluid inclusion composition and graphite crystallinity

Both the fluid inclusions and the graphite mineral inclusions are hosted exclusively in the inclusion-rich core of the analyzed garnet (population (2), sample 19WM118) which is enveloped in an inclusion-free rim (population (3); Fig. 11a). Graphite is absent from the rock matrix. This distribution suggests that the analyzed inclusions are primary in origin and were trapped during the early stages of garnet growth.

Visual estimation of the volumetric phase ratios in the fluid inclusions was challenging owing to the relatively high refractive index of garnet and the small inclusion size, which rendered many of the inclusions too dark to clearly observe the phase assemblage. However, in some inclusions the three-phase assemblage of aqueous liquid, carbonic liquid and vapor was identifiable by observing the motion of the vapor bubble, which "rattled" inside the carbonic liquid portion (Fig. 11b). In all such inclusions, the carbonic liquid fraction occupies the highest proportion of the inclusion volume at ~80 vol.%, whereas the outer aqueous liquid occupies ~15 vol.% and the innermost vapor bubble occupies ~5 vol.% (Fig. 11b). These estimated volume fractions were consistent between all analyzed inclusions, suggesting that the inclusions are unmodified and preserve the composition and density of the trapped fluid.

Raman spectroscopic analysis of the fluid inclusions showed that the OH-stretching band of H_2O is essentially the same as pure H_2O (Fig. 11b; Sun et al., 2010), which indicates very low to negligible salinity of the aqueous liquid. In addition to the Raman peaks of the Fermi diad of CO_2 fluid, we also observe relatively strong Raman peaks at ~1276 and 1384 cm^{-1} indicative of molecular CO_2 dissolved in the aqueous fluid (Fig. 11b; Frezzotti *et al.,* 2012). The Fermi diad itself overlaps somewhat with these latter peaks, and repeat analyses showed variable peak splitting (Δ) ranging from ~103 to 104.2 cm^{-1}, indicating carbonic fluid densities of both vapor (~0.2 g/cm^3) and liquid CO_2 (~0.7 g/cm^3), consistent with our visual observations (Fig. 11b). It should be noted that the vapor bubble generally moved around too rapidly to allow for targeted analysis of either liquid or vapor CO_2 independently, so each analysis likely sampled both fluids simultaneously. Nevertheless, by incorporating the visually estimated relative volume fractions of carbonic liquid and vapor, we were able to estimate the overall CO_2 density of ~0.68 g/cm^3, a bulk composition of 60 mol.% CO_2 + 40 mol.% H_2O, and a total bulk density of 0.80-0.85 g/cm^3.

We conducted isochoric modeling of the fluid inclusions based on the above constraints and using an estimated temperature range of 550-600 °C (Fig. 11c; solvus curve for an H_2O-CO_2 fluid of 60 mol.% CO_2 is reproduced from Connolly & Bodnar, 1983). Projection of the relevant fluid isochores to this temperature range yields a maximum pressure estimate of ~3.7 kbar at 600 °C (Fig. 11c).

The activities of H_2O and CO_2 were estimated based on the above constraints, as well as using the data of Aranovich and Newton (1999). An activity of H_2O of ~0.5 was obtained for an H_2O-CO_2 fluid of 60 mol.% CO_2 at 600 °C and 4 kbar (Fig. 11d). We acknowledge that such low water activities are unlikely to be related to the presence of graphite alone (Connolly & Cesare, 1993), particularly during the mineral dehydration associated with progressive garnet growth (Pattison, 2006). However, we highlight that garnet across the Kluane Schist typically hosts mineral inclusions of calcite (Figs. 6c and S6), suggesting the presence of calcite and/or a carbonate-rich fluid during early garnet growth. Recent Ramen spectroscopy of garnet fluid inclusions associated with the presence of a carbonate-rich fluid produce aH_2O values in line with our own (0.1–0.65; Bader *et al.,* 2014).

Our Raman spectroscopic results of graphite mineral inclusions consistently show a strong, pronounced G band and only a weak to nearly absent D1 band (Fig. S1), indicative of relatively high temperature graphite (Beyssac et al. 2002). Based on the relative integrated intensities of the two latter Raman bands and using the calibration equation provided by Beyssac et al. 2002, we obtain temperature estimates ranging from 500 to 630 °C (Fig. S1).

5. Metamorphic sequence and pressure-temperature conditions

5.2. Mineral reactions

The limited variation in Kluane Schist bulk chemistry indicates the differences in mineral assemblage and chemistry are largely the result of changing metamorphic conditions. In the following section we document the sequence of reactions pertaining to these changing conditions that resulted in our observed paragenesis across the Kluane Schist.

5.2.1. Zone 1: development of bedding parallel fabrics (S_1)

The S_1 bedding parallel fabrics comprise chlorite–muscovite–titanite–calcite (Fig. 5b). Initial albitic porphyroblasts, which overgrow S_1, are likely stabilised by the less calcic whole rock compositions typical of zone 1 (Fig. 9b). As albite porphyroblasts typically preserve S_1 oriented muscovite, titanite and chlorite and lack of chemical zonation (*e.g.,* Figs. 5b and 9i), they likely grew while both calcite and titanite remained stable. As such, these albite porphyroblasts along with their associated S_1 fabric document initial Kluane Schist metamorphism at conditions around prehnite-pumpellyite to greenschist transition, where albite is considered to form during the breakdown of zeolite-facies clays (*e.g.,* Bishop, 1972, Coombs *et al.,* 1976, Utada, 2001, metamorphic mineral abbreviations from "The Canadian Minerologist list of symbols for rock- and ore-forming minerals" updated December 30, 2019 and accessed from: https://www.mineralogicalassociation.ca/wordpress/wp-content/uploads/2020/01/symbols.pdf)

Zeolite-facies clays = ab + H_2O [1].

5.2.2. Zone 2a: Zoisite-in and initial biotite growth

Zoisite is associated with graphite-rich domains, calcite and titanite (Fig. 5c). Zoisite is typically aligned with the S_{2a} fabric and is observed to directly replace calcite within the lower-grade regions of zone 2 (Fig. 5c). Calcite and titanite are lost from the assemblage just upgrade of zone 1 (Figs. 4 and 5c, d). Ilmenite and rare hematite are present. At slightly higher grades biotite enters the assemblage and holds a similar microstructural position to zoisite (Fig. 5d). The appearance of biotite is associated with a reduction in chlorite abundance (Fig. 5b *versus* d). Combined these observations suggest zoisite growth and initial biotite production via:

$$ttn + 3ms + 2chl + 15cal + 23qtz = 3bt + 8zo + 12H_2O + 15CO_2 + ilm \quad [2].$$

5.2.3. Zone 2b: Continued growth of biotite

Towards the higher-grade regions of zone 2 progressive biotite growth is most likely supported by the tschermaks exchange associated with the recrystallisation of S_1-oriented chlorite and muscovite (*e.g.,* Figs. 5d and 9f, g; Ernst, 1963, Ramsay, 1973, Pattison, 1987):

$$ms_{(1)} + chl = bt + ms_{(2)} + qtz + H_2O \quad [3].$$

[3] accounts for the second population of S_{2a} oriented muscovite wrapping zoisite and the distinct change in muscovite chemistry between zones 1 and 3 (*i.e.,* $ms_{(1)}$ and $ms_{(2)}$; Figs. 5d and 9f, g).

5.2.4. Zone 3: garnet-in

The lowest grade assemblage within zone 3 comprises course, euhedral garnet which hosts inclusions of zoisite, graphite, calcite and S_1 aligned quartz (Fig. 6c). Plagioclase shows a similar microstructural character, with their cores containing inclusions of calcite, zoisite and S_1 aligned muscovite and chlorite (Fig. 6b). Both garnet and plagioclase show partial wrapping by the S_{2a} fabric (Fig. 6b, d). Within these lower-grade zone 3 assemblages zoisite shows a decreased abundance in the matrix compared with zone 2. The similar textures preserved by zone 3 garnet and plagioclase, their similar microstructural position, and shared Ca-rich core chemistry (*e.g.,* Figs. 5 b, c, d, 9i and Table S9) suggests they likely developed coevally at the expense of zoisite (*i.e.,* [4]; *cf.* Goto *et al.,* 2002). Upgrade within zone 3, zoisite is rapidly lost from the assemblage (*e.g.,* Fig. 6c *versus* 6d) and garnet preserves progressive growth zonation moving to less grossular-rich and more Mg/(Mg + Fe) rich chemistries (Table S9). These higher-grade zone 3 assemblages also show a marked decrease in chlorite and muscovite (*e.g.,* Fig. 6d). Combined these observations suggest the continued growth of garnet likely occurred at the expense of both chlorite and muscovite:

4 zo + qtz = 5an + grs + 2H_2O [4] (after: Goto *et al.,* 2002).

and

ms + chl + qtz = grt + bt + H_2O [5].

In AFM space, the increase in chlorite Mg/(Mg + Fe) between zone 1 to zone 3 mirrors the core to rim evolution of garnet compositions (Figs. 9c, 12a and Table S9). This serves to destabilise chlorite with respect to the Kluane Schist bulk composition and promote the growth of garnet and biotite (Fig. 12a; *i.e.,* [5] as the bulk compositions now lie closer to the garnet-biotite tie line). Partial wrapping of garnet by biotite-rich S_{2a} fabrics (*e.g.,* Fig. 6d) further implies the production of biotite coeval with this period of garnet growth (*cf.* S_1 *vs.* S_{2a} in Fig. 6d).

5.2.5. Zone 4: staurolite-in

Chlorite abundance is significantly reduced immediately upgrade of the first appearance of staurolite (*cf.* Figs. 4 and 3g). This implies initial staurolite production at the expense of chlorite:

ms + chl + qtz = st + bt + H_2O [6] (*e.g.,* Pattison & Tinkham, 2009)

However, as chlorite abundance is limited within zone 4 and staurolite is typically observed as abundant, coarse and euhedral porphyroblasts (*e.g.,* Fig. 3g), it is unlikely that reaction [6] accounts for total staurolite production across the Kluane Schist. Instead, the common association between staurolite and the cloudy, embayed and corroded garnets typical of zone 4 suggests their involvement in the production of staurolite (Fig. 3g; *e.g.,* Dempster *et al.,* 2017). Garnet rims within these staurolite bearing assemblages (population (2) above) typically preserve evidence for resorption coupled with a sharp decrease in Mg/(Mg + Fe) (Table S9). This is consistent with their consumption during the growth of the Mg-rich staurolite typical of the Kluane Schist:

chl + grt + ms = st + bt + qtz + H_2O [7].

This reaction is expressed as a tie line flip in AFM space (Figs. 12b) and is consistent with the development of the biotite-rich S_{2b} fabrics typical of zone 4 (Fig. 3g).

5.2.6. Zone 5: aluminosilicate-in

Within the lower grade regions of zone 5, knotty anhedral porphyroblasts of andalusite are locally intergrown with the S_{2b} fabric and quartz (Fig. 6e). Andalusite hosts inclusions of staurolite, biotite and muscovite (Fig. 3e and 6e). Within these lower-grade zone 5 rocks, staurolite persists as the major porphyroblast and the S_{2b} fabric shows a decrease in muscovite compared with zone

4 (Fig. 6e). Chlorite is absent from the prograde assemblage (Fig. 6e). These observations point to initial andalusite growth via:

ms + chl + qtz = and + bt + H_2O [8]

Further andalusite growth within higher-grade zone 5 samples is observed to occur directly at the expense of the zone 4 assemblage staurolite–biotite–muscovite–quartz (*e.g.,* Fig. 3e). The resulting assemblage lacks the staurolite porphyroblasts seen downgrade. Instead staurolite occurs included within andalusite along with biotite, quartz, and rare muscovite (Fig. 3e). Population (3) inclusion-free garnet is also observed both as mantles to cloudy population (2) garnet and as finer, individual crystals (Fig. 6f). These distinct, low Ca-garnets (*e.g.,* Fig. 10) are typically associated with graphite-free plagioclase, andalusite and sillimanite (Fig. 6f). Combined these observations imply continued aluminum silicate growth at the expense of staurolite and muscovite (Fig. 12c):

ms + st = and/sil + grt + bt + qtz + H_2O [9].

Reaction [9] likely superseded [8] when the limited chlorite was exhausted from the lowest grade rocks of zone 5. However, the persistence of relic staurolite throughout zone 5 suggests underlying kinetic controls may also play a role (*e.g.,* Pattison & Tinkham, 2009).

Upgrade within zone 5, fibrolitic sillimanite appears in more biotite-rich and less muscovite-rich S_{2b} fabrics, plagioclase grew graphite-free tips, and andalusite is replaced by muscovite (*e.g.,* Fig. 6f). The direct replacement of andalusite by fibrolitic sillimanite and inclusion of population (3) garnet in plagioclase, both suggest fibrolitic sillimanite growth postdates [9] (Fig. 6f). Fibrolitic sillimanite growth likely occurs through a combination of three distinct reactions, accounting for its close association with the biotite-rich S_{2b} fabric (*cf.* Carmichael, 1969):

a) and + qtz = ms [10],

b) bt = ab [11],

c) ms + ab = sil (fib) + bt + qtz [12],

resulting in the overall polymorph transformation:

and = sil (fib) [13].

Within the south-central regions of the Kluane Schist, a local assemblage contains prismatic sillimanite and is devoid of staurolite (sample 245b in Figs. 2 and 7a). Coarse, euhedral garnet is wrapped by biotite-rich S_{2b} fabrics and prismatic sillimanite (Fig. 7a). Garnet cores host inclusions of aligned quartz, biotite, and graphite while garnet rims domains lack inclusions (Fig. 7a). This distinct assemblage was likely the result of [9] moving to completion, where the kinetic barriers required for total staurolite consumption and were sufficiently lowered by the local presence of a fluid (*e.g.,* Pattison & Tinkham, 2009).

5.2.7. Zone 6: Cordierite-in

Zone 6 is marked by the appearance of cordierite across the Kluane Schist (Fig. 7b). Within lower-grade units cordierite is primarily associated with the biotite-muscovite S_{2b} fabric and largely uncorroded andalusite and staurolite porphyroblasts (Fig. 7b). Coincident with the appearance of cordierite, muscovite shows a significant decrease in abundance and biotite shows recrystallization to more K-rich, less Mg/(Mg + Fe) chemistries (Figs. 7b, 9c and 12d). These observations suggest the initial growth of cordierite occurred primarily at the expense of muscovite coupled with an increase in the Tschermak component of biotite (Figs. 9e and 12d; *cf.* Ikeda, 1998):

$bt_{(1)} + ms = \text{Mg-rich } crd + bt_{(2)} + qtz + H_2O$ [14]

where:

$bt_{(1)}$ = K-poor, Mg/(Mg/Fe)-rich biotite (Fig. 9c, e);

$bt_{(2)}$ = K-rich, Mg/(Mg/Fe)-poor biotite (Fig. 9c, e)

In AFM space, this shift in biotite composition can also be inferred to destabilise both garnet and aluminium silicate at the expense of cordierite (Fig. 12d). In thin section, we observe the direct replacement of garnet and fibrolitic sillimanite by cordierite (*e.g.,* Fig. 7c). Moving up-grade though zone 6, cordierite abundance progressively increases while fibrolitic sillimanite decreases, until it is only observed as inclusions to cordierite (Figs. 7b *versus* 7c *versus* 3c). Within the highest-grade units of zone 6, garnet cores are preferentially replaced (atolled) and garnet rims show high-Mn, low-Mg chemistries consistent with resorption (Figs. 3c, 10 and Table S9). These observations are in accordance with:

2 grt + 4 sil + 5 qtz = 3 crd [15]

Reaction [15] is likely limited by the kinetic barriers associated with the sluggish dissolution of refectory garnet porphyroblasts (*e.g.,* Pattison & Tinkham, 2009). However, fluid produced by the dehydration reaction [14] (Ikeda, 1998) could potentially act as catalyst to [15]. Microstructural and chemical evidence suggests garnet dissolution is common within zone 6 (*e.g.,* Figs. 7c, 10 and Table S9). We therefore suggest the coeval occurrence of both [14] and [15], which together likely account for the observed abundance of cordierite across the Kluane Schist.

5.2.8. Zone 7: Migmatisation

The paleosome assemblage of zone 7 consists of biotite–plagioclase–cordierite–quartz–K-feldspar +/- garnet–sillimanite (Fig. 7e). Staurolite occurs as relic metastable porphyroblasts and retrograde muscovite is randomly oriented (Fig. 7e). Leucosome domains comprise cordierite–quartz–plagioclase–muscovite (Fig. 7f) and are distinct in composition from the granodioritic Ruby Range Batholith (K-feldspar–biotite–plagioclase–quartz +/- hornblende; *e.g.,* Israel *et al.,* 2011a, b). This suggests zone 7 leucosome does not represent injectate from the nearby Ruby Range Batholith. Peritectic K-feldspar and cordierite occur at the expense of S_{2b}-oriented biotite and fibrolitic sillimanite within the paleosome (Fig. 7e). This suggests the leucosome most likely represents the product of in-situ melting via the biotite dehydration reaction (*e.g.,* Le Breton & Thomson, 1988):

bt + sil + qtz = kfs + $crd_{(2)}$ + melt [16].

Further evidence of this reaction is provided by the decreased abundance of biotite and fibrolitic sillimanite within zone 7 (*e.g.,* Fig.7c *versus* 7e).

5.3. **Pressure–temperature conditions of metamorphism**

Combining our above reactions and microstructural observations, the metamorphic history of the Kluane Schist can be summarised as two distinct events, M_1 and M_2. The first, M_1, is expressed as S_1 bedding-parallel chlorite–muscovite–calcite–titanite fabrics (*e.g.,* Fig. 5a, b). With the second, M_2, accompanying the progressive development of a transposition foliation that includes an earlier phase, S_{2a}, defined by chlorite–muscovite +/- biotite–zoisite fabrics that becomes fully transposed into a pervasive, planar, biotite-rich S_{2b} foliation (*e.g.,* Figs. 3, 5c, d and 6). At higher metamorphic grade the transposition fabric consists of a cm-spaced, biotite–cordierite and plagioclase–quartz (+/- melt–garnet–sillimanite) gneissic fabric (*e.g.,* Figs. 3 and 4).

5.3.1. Forward modelling

As the bulk composition of the Kluane Schist only shows a limited variation and no consistent trend with grade (*e.g.,* Fig. 9a, b), our calculated phase diagram considers a single average bulk composition encompassing all XRF analyses across the Kluane Schist. Our resulting phase diagram uses ds5.5, its associated activity models and combines four regions of varying aH$_2$O which we consider to best account for the evolution of aH$_2$O during the metamorphism of the Kluane Schist (*cf.* Figs. 11 and 13). Our inferred evolution of aH$_2$O was constrained using the results of Raman spectroscopic analysis (see above; Fig. 11), forward petrological modelling (Fig. 13), thin section observation and the assumption of increasing aH$_2$O during prograde metamorphism due to progressive dehydration (*e.g.,* Pattison, 2006). Raman spectroscopic analysis of the fluid-inclusion rich garnet domains typical of zones 3–4 suggests their mineral assemblages developed under a reduced aH_2O of 0.5 (Figs. 3g, 6c, d and 11). This low aH_2O value is supported by the presence of calcite mineral inclusions within garnet (*e.g.,* Figs. 6c and S6). The cordierite-free, andalusite/sillimanite–garnet–biotite (+ quartz, plagioclase, ilmenite; *e.g.,* Figs. 3e and 6e) assemblage typical of zone 5 requires an aH_2O < 0.65 (Fig. 13). This result is further supported by *P*–*T* estimates from a zone 5 sample (Fig. 13; all *P-T* results found in Table 1). We therefore set aH_2O = 0.55 for the *T* region associated with zone 5 assemblages (Fig. 13). Upgrade of zone 5, the cordierite–biotite +/- sillimanite–garnet (+ quartz, plagioclase, ilmenite; Figs. 3c and 7c) assemblage typical of zone 6 is produced at all values of aH_2O (Fig. 13). Therefore, to account for the increased aH_2O associated with prograde dehydration (*e.g.,* Pattison, 2006), we set aH_2O = 0.95 for *T* regions where graphite is present (< 630ºC; Fig. S1; Connolly & Cesare, 1993) while within graphite-free assemblages we assume aH_2O ~ 1 (Figs. 13 and S1; Connolly & Cesare, 1993).

The resulting phase diagram (Fig. 14) is not a perfect representation of the phase relationships we observe, producing several inconsistencies compared with our petrological observations. These include: (1) the prediction of titanite with zoisite-bearing assemblages, where instead we typically observe ilmenite +/- hematite (*cf.* Fig. 4). This likely arises from an inaccurate definition of XFe^{3+} within our model system (see section 3.2; Forshaw & Pattison, 2021). (2) the prediction of clinozoisite (cz) within zone 1 assemblages. This likely results from the heightened XCa within the input bulk composition compared with that typical for zone 1 (*cf.* Fig. 9b). (3) muscovite is predicted to leave the assemblage prior to chlorite and significantly downgrade of zone 6, where it is observed in prograde fabrics (*cf.* Figs. 4 and 7b). (4) staurolite is observed to occur with both aluminium silicate and cordierite, which is not predicted by our model (*e.g.,* Figs. 4, 6e and 7b). Thin section observations suggest these inconsistencies mostly likely relate to disequilibrium processes, in particular the sluggish dissolution of porphyroblasts such as staurolite and garnet (*e.g.,* Pattison & Tinkham, 2009, Pattison & Spear, 2018).

These inconsistencies aside, the overall topology of our model is consistent with the observed order of index mineral paragenesis as observed across the Kluane Schist (*cf.* Figs. 2, 4 and 14). Further, we also see good agreement between our forward modelling and independent *P*-*T* estimates provided by thermobarometry (discussed further in the next section; Fig. 14 and Table 1). Equally, in comparison with the other combinations of dataset and activity-composition models outlined in section 3.2, which include ds6.2 of Holland & Powell (2011) coupled with the metapelite HPx-eos of White *et al.,* (2014) and the modified SPaC14 dataset of Spear & Cheney (1989) with activity models as described in Pattison & Debuhr (2015), our resulting ds5.5 model is more in line with natural phase observations (Figs. S3 and S4). Finally, the use of ds5.5 without varying aH_2O does not produce a result aligned with our thermobarometry or thin section observations (Fig. S2). We therefore consider our resulting model (Fig. 14) as the best approximation for quantifying the *P*-*T* conditions experienced during the metamorphic evolution of the Kluane Schist.

5.3.2. Thermobarometic estimates

Av*P* estimates below zone 5 were constrained using a range of aH_2O (0.3, 0.4, 0.5, and 0.6; Table 1). We see a limited variability of +/- 0.46 kbar when considering different aH_2O within a single equilibrium assemblage (Table 1). Within zone 3, we chose an aH_2O value of 0.5 to remain consistent with the results of garnet fluid inclusion analysis and our forward modelling (*e.g.,* Figs. 11 and 14). Above zone 5, Av*P* is completed with $aH_2O = 1$ due to the largely graphite-free nature of the rock matrix (Fig. 7b, c and Table 1). Av*P* on migmatite units within zone 7 is completed with an aH_2O of 0.4 and 1, showing a limited variation of +/- 0.3 kbar between results (Table 1). We choose a value of 0.4 to remain consistent with the reduced aH_2O commonly suggested for pelitic migmatites (*e.g.,* Phillips, 1981, Lamb & Valley, 1988, Waters, 1988, Giorgetti *et al.,* 1996, Bader *et al.,* 2014, Waters, 2019). Our conventional barometry estimates, which assume aH_2O = 1 (see section 3.3; Wu *et al.,* 2015, 2017), are considered reliable due to the lower susceptibility of a single barometer equilibria to changes in aH_2O (*e.g.,* Waters, 2019). Results from conventional barometry and Av*P*, where completed on the same sample, are within 1-sigma error of one another (Fig. 14 and Table 1).

5.3.3. Field gradient for the Kluane Schist

Combining the results from our phase diagram, Av*P*, and conventional barometry calculations we can constrain the main phase of Kluane Schist metamorphism (M_2) to between ~3 kbar at 375 °C and 4.0–4.5 kbar at 700-750 °C, defining a field gradient of ~200 °C/kbar or ~55 °C/km (assuming a crustal density of 2.8 g/m^3) across the Kluane Schist (Fig. 14). These conditions largely align with other Buchan-style terranes worldwide, falling within the range of recent estimates for the Wopmay Orogen Buchan sequence (34–68 °C/km; St-Onge & Davis, 2017), close to estimates for progressive Buchan-style metamorphism across the western Pan-African Kaoko belt, Namibia (~50 °C/km; Will *et al.,* 2004), and in line with the staurolite–andalusite–sillimanite sequences that define the western Buchan domain of northeast Scotland (~3.5 kbar at 550 °C and 4.0–4.5 kbar at 700–750 °C; Pattison & Goldsmith, 2022). Integrating these results with our structural analysis, we observe the progressive intensification of deformation coinciding with increased metamorphic grade as you go from the core of the Kluane Schist towards its northern, eastern, and southwestern edges (Figs. 2 and 3). To the north and east we define an inverted metamorphic sequence between the greenschist facies and amphibolite-granulite transition while to the south a correct way up sequence culminates at staurolite-grade before exposure is lost under Kluane Lake (Figs. 2 and 3). Together these results suggest M_2 is reflected through the development of a Buchan-style metamorphic sequence between lower-grade zone 2 assemblages and higher-grade zone 7 assemblages (Fig. 14).

6. Discussion

6.1. Comparison with previous studies

Previous evaluation of the metamorphic conditions experienced by the Kluane Schist suggest it underwent two distinct episodes of metamorphism; an early regional event, peaking at T ~510 °C and P ~ 7 kbar, and a subsequent contact metamorphic episode at T ~ 530–720 °C and P ~ 3.5–4.5 kbar (Erdmer, 1991, Mezger *et al.,* 2001). In contrast, our findings suggest initial burial metamorphism of the Kluane Schist was limited to the sub-greenschist-facies (P <<4 kbar; Fig. 14) while its subsequent high–T, low–P metamorphism reflects a regional Buchan-style event coeval with deformation (Figs. 3, 4 and 14). The conditions we record for this second event are similar to those suggested by Mezger *et al.,* (2001) (T ~400–750 °C & P ~ 3.0–4.5 kbar; Fig. 14, Table 1), but we do not attribute it to a static overprint by a 5-6 km wide contact aureole. We discuss these inconsistencies further below.

6.1.1. *Pressure–temperature conditions of M1:* To obtain the P-T conditions for M_1, Mezger *et al*. (2001) consider a single zoned garnet in equilibrium with reversely zoned plagioclase (core Xan = 0.24; rim Xan = 0.36). Their resulting M_1 P-T path involves significant decompression across a limited range of temperatures (cores ~7.5 kbar at 510 ºC to rims ~ 3.5 kbar at 550 ºC;

Mezger *et al.,* 2001). We note several inconsistences between such a P-T trajectory and the observed phase relationships across the Kluane Schist. First, garnet cores overgrew a lower-grade fabric (S_1; muscovite–chlorite–graphite Figs. 5b and 6c) than which they are partially wrapped by (biotite-rich S_{2a}; Fig. 6c, d). Second, the euhedral shape of garnet crystals within zone 3 (*e.g.,* Fig. 6c, d), their preserved zonation patterns (Table S9) and intra-sample crystal size distribution (Fig. 6d) are all more consistent with garnet growth during increasing P and T rather than isothermal decompression (*e.g.,* Pattison & Tinkham, 2009, George & Gaidies, 2017). Third, we do not observe evidence of a distinct higher-pressure mineral assemblage (*e.g.,* kyanite) associated with garnet cores or indeed elsewhere across the Kluane Schist. Fourth, we do not observe chemical or microstructural evidence for the overprinting of mineral assemblages that may be related to significant decompression (*cf.* Vice *et al.,* 2020). Finally, the highest-P estimates provided by Mezger *et al.,* (2001) (~7.5–7.0 kbar) were calculated using grossular-rich garnet in equilibrium with inferred oligoclase cores (Xan = 0.32–0.24); these plagioclase compositions contrast with the measured garnet-grade plagioclase compositions reported by Mezger *et al.,* (2001) (Xan = 0.37–0.31) and those within this study (Fig. 9h, i). Instead, the zone 3 plagioclase we observe typically shows normal zonation with individual grains characterised by more anorthite-rich cores than that suggested by Mezger *et al.,* (2001) (Xan = 30–40; Figs. 6b, d and 9h, i). Microstructural relationships suggest these more anorthite-rich plagioclase cores represent part of the same mineral assemblage as the grossular-rich garnet cores (*e.g.,* Fig. 6b, c, d).

We instead suggest the development of these Ca-rich mineral cores (*i.e.,* garnet, plagioclase) reflects fluid infiltration and/or variation in local composition rather than elevated pressures. This is evidenced by the distinct increase in whole rock Ca/(Ca + Na) upgrade of zone 1 (*e.g.,* Fig. 9b, h), the calcite inclusions typical of garnet within zone 3 (*e.g.,* Figs. 6c and S6), and the low $a\mathrm{H_2O}$

values that are suggested during the initial growth of garnet (Figs. 11, 13 and 14; *e.g.,* Connolly & Cesare, 1993, Bader *et al.,* 2014). As such our zone 3 pressure estimates (~3.0–3.5 kbar; Fig. 14 and Table 1) are derived from an assumed equilibrium between the outer core domains of garnet and plagioclase with matrix phases chlorite–biotite–muscovite (+H_2O, quartz) (*cf.* Fig. 6d).

6.1.2. M_2: contact versus regional metamorphism. Mapped isograds relating to M_2 highlight a hot-side-up, inverted metamorphic field gradient which increases in grade towards the Ruby Range Batholith (Figs. 2 and 3, this study; Fig. 2 in Mezger *et al.,* 2001). Coincidence between this field gradient, the location of the Ruby Range Batholith, and evidence for the static growth of the staurolite–aluminium-silicate–cordierite M_2 mineral sequence led Mezger *et al.,* (2001) to suggest M_2 primarily reflected an extensive ~5–6 km contact aureole to the batholith. However, within this study we document the consistent entrainment of M_2 index minerals within prograde transposition fabrics of the Kluane Schist, where metamorphic grade appears directly related to the intensity and style of the deformational fabric preserved (Figs. 3, 4, 5, 6 and 7). We further highlight this coupled metamorphic-deformational relationship is not unique to the northern regions of the Kluane Schist (*e.g.,* Figs. 2 and 3). We additionally documented a correct way up metamorphic sequence, to at least staurolite-grade (zone 4), along the southeast of Kluane Lake (Figs. 2 and 3). This is inconsistent with static staurolite growth within an aureole to the Ruby Range Batholith as you would expect the metamorphic grade to decrease with distance away from the batholith. Combined these observations suggest M_2 was a regional metamorphic event that occurred coeval with evolving deformation conditions rather than related to static recrystallisation during contact metamorphism (*e.g.,* Figs. 2, 3 and 4)

6.2. Tectonic evolution of the Kluane Schist

Pervasive deformation and metamorphism have largely obscured the evidence relating to the depositional environment of the Kluane Schist, with both a back-arc (*e.g.,* Eisbacher, 1976, Lowey, 1992, Mezger *et al.,* 2001) and forearc (McClelland & Saleeby, 1992, Israel *et al.,* 2011a, Canil *et al.,* 2015, Waldien *et al.,* 2021b) setting inferred during its deposition. Our data provides new constraints on the style of Kluane Basin inversion. Below we summarise the metamorphic and structural evolution of the Kluane Schist within the context of Mesozoic Cordilleran orogenesis.

D1M1: After its deposition in Late Cretaceous time, the Kluane Schist experienced D_1M_1 which is expressed as the S_1 chlorite–muscovite–titanite–calcite fabric within its lowest-grade zone 1 units (*e.g.,* Fig. 5a, b). Although the metamorphic conditions are difficult to quantify for M_1, the preserved S_1 assemblage suggests M_1 occurred around the prehnite-pumpellyite to greenschist transition (*P-T*: ~2–4 kbar, ~250–350 °C; Fig. 14).

The low-*P* conditions we record for M_1 suggest that the Kluane Schist only experienced limited tectonic burial at this time, likely during the waning stages of Insular terrane accretion to the western continental margin. As such, we suggest D_1M_1 reflects the initial stages of Kluane Basin collapse between the encroaching Insular terranes and the previously accreted Intermontane terranes, leading its initial underthrusting below the Yukon-Tanana terrane, which was part of the North American plate within southwest Yukon at this time (*e.g.,* Mezger *et al.,* 2001, Israel *et al.,* 2011a, Nelson *et al.,* 2013, Box *et al.,* 2019).

D2M2: The second and most intense period of metamorphism experienced by the Kluane Schist was coeval with a period of NE-SW compression. D_2M_2 was largely responsible for the development of the metamorphic field gradient preserved across the Kluane Schist along with its petrologic zones (Fig. 2). D_2M_2 involved the transposition of greenschist-grade S_1 fabrics through

S_{2a} orientations, and culminating in a penetrative S_{2b} folia at staurolite grade (Fig. 3). D_2M_2 is associated with symmetric F_2 folds which become progressively tighter with metamorphic grade, and eventually isoclinal at staurolite grade, with their axial planes parallel to S_{2b} fabrics (Fig. 3h, f). Rootless and isoclinal F_{2b} folds were progressively sheared to form a coarsened and fully transposed S_{2b} gneissosity within andalusite and cordierite grade units (*e.g.,* Fig. 3b, d, f). This lockstep between metamorphic assemblage and fabric development strengthens our interpretation of a coupled metamorphic-deformational field gradient across the Kluane Schist, while illustrating how the deformation occurred within an evolving strain field (*e.g.,* Figs. 3 and 4).

During D_2M_2 lower-grade assemblages were deformed within a dominantly coaxial strain field while higher-grade assemblages show a predominance of non-coaxial strain (Figs. 3, 4, 5, 6 and 7). This evolving strain field likely tracks the initial burial below and subsequent override of the Kluane Schist by Yukon-Tanana terrane (*e.g.,* Israel *et al.,* 2011a); initial flattening deformation occurred as the Kluane Schist underwent initial tectonic burial below Yukon-Tanana terrane, with the evolution to a non-coaxial stain field recording the subsequent WNW- to W-directed wholesale override of the Kluane Schist by the Yukon-Tanana terrane (*e.g.,* Israel *et al.,* 2011a). This accounts for the diachronous style of metamorphism and deformation recorded by D_2M_2 and development of the dominant WNW-striking, largely NNE-dipping S_{2b} transposition fabric across the Kluane Schist (Figs. 1b and 2). The structures, field gradient, and strain evolution preserved throughout D_2M_2 are consistent with their development during a period of largely orogen-normal compression, such as that hypothesised during the terminal accretion of the Insular terranes (*e.g.,* the 120-60 Ma period of Monger & Gibson, 2019).

D3: D_3 lacks the development of a planar fabric. Instead, the formation of L-tectonites with mineral alignment lineations defined by tourmaline, mica, and plagioclase suggests a shift to a

SW-directed non-coaxial strain field. This non-coaxial strain field is best demonstrated through the folding of S_{2b} fabrics to form F_3 shear folds (*e.g.,* Fig. 8). F_3 folds show consistent vergence towards the SW and trend to the SE, suggesting D_3 occurred during a period of NE-SW compression (Fig. 8a). Asymmetrical lensoidal quartz stringers and boudins observed parallel to mineral alignment lineations also show a strong tops-to-the-WSW and SW shear sense (*e.g.,* Figs. 3a and 8b).

The consistency in trend between F_2 and F_3 folds suggests that both D_2 and D_3 demonstrate a similar NE-SW-directed contractional event, likely resulting from override of the Kluane Schist by the Yukon-Tanana terrane. However, the SW-directed shear recorded during D_3 is distinct from that during D_2 (see above, *e.g.,* Figs. 3 *versus* 8). The shift to D_3 likely coincides with the overall change in Northern Cordilleran tectonics, from one of orogen-normal compression to one dominated by orogen-parallel strike-slip faulting (*e.g.,* post- *ca.* 60 Ma, Monger & Gibson, 2019). During this period, the North American craton is considered to have migrated southwestwards (*e.g.,* Kent & Irving, 2010, Monger & Gibson, 2019) and likely imparts this motion on the accreted Yukon-Tanana terrane, accounting for the dominant SW-verging shear structures preserved across the Kluane Schist during D_3. As this shift in craton trajectory is most likely gradual (*e.g.,* Monger & Gibson, 2019), it seems reasonable that both the latter stages of D_2 and D_3 reflect override of the Kluane Schist by Yukon-Tanana terrane, albeit reflecting changes in the stress field in response to the direction of the migrating North American craton.

D4: The final episode of deformation expressed across the Kluane Schist relates to the formation of F_4 buckle folds (F_4 in Fig. 2). The buckled nature of these folds implies D_4 occurred when the Kluane Schist was cooler than during D_2 or D_3. These folds trend E-W, suggesting D_4 occurred during a N-S period of compression. As such, D_4 likely occurred coeval with Kluane

Schist exhumation, producing the larger-scale fold pattern of our mapped petrologic zones and isograds (Fig. 2).

Considering the above, we view the Kluane Basin as a Late Cretaceous depocenter (*ca.* 94 Ma; Israel *et al.,* 2011a) that was open during the late stages of Insular terrane accretion. This accounts for the metamorphic evolution of the Kluane Schist only involving a shallow underthrusting below the continental margin prior to its wholesale override by Yukon-Tanana terrane. As such, metamorphism of the Kluane Schist was primarily driven by initial limited burial below and subsequent override by a thermally mature Yukon-Tanana terrane, which is considered to have hosted significant magmatic activity during the Cretaceous (*e.g.,* the Tanacross–Dawson Range belt and Tok–Tetlin belt of Hart *et al.,* 2004; and the '100–50 Ma magmatic belt' of Gehrels *et al.,* 2009). This model provides a potential mechanism to develop the heightened geothermal gradient implied by the low-medium pressure, high temperature metamorphic regime we record across the Kluane Schist, while also accounting for the evolution of flattening to rotational fabrics and the development of higher-order structures preserving regional tops-to-the-SW shear (*e.g.,* Israel *et al.,* 2011a).

6.2. **Tectonic significance of the Kluane Schist within the Southwest Yukon**

Evaluation of the metamorphic conditions experienced by the Blanchard River assemblage to the south of the Kluane Schist (*e.g.,* Fig. 1b) suggest it underwent two distinct episodes of regional metamorphism; an early Barrovian event, peaking at T ~ 650 °C and P ~ 6.5 kbar, followed regional exhumation and subsequent metamorphism at P ~ 3 kbar (Vice *et al.,* 2020). In contrast, the conditions and mineral assemblages we record across the Kluane Schist suggest it experienced initial metamorphism within the sub-greenschist-facies (our D_1M_1 above; Fig. 14) followed by a Buchan style event which peaked at ~700–750 °C and 4.0–4.5 kbar (our D_2M_2 above; Fig. 14). The initial high-*P* kyanite–garnet grade assemblages observed across the Blanchard River assemblage, along with their lower–*P* cordierite–andalusite/sillimanite–spinel coronas (Vice *et al*., 2020) are never observed across the Kluane Schist. Instead, the cordierite–aluminium silicate assemblages we document across the Kluane Schist appear associated with its main phase of metamorphism, without evidence for these assemblages having overprinted a previous higher-*P* event (*e.g.,* Figs. 3, 6, 7). These observations suggest that the initial Barrovian event recorded across the Blanchard River assemblage (Vice *et al*., 2020) was not experienced by the Kluane Schist.

Our interpretation does not preclude the potential for a later shared metamorphic history between the Kluane Schist and the Blanchard River assemblage. Both units preserve evidence for a distinct low–*P*, high–*T* metamorphic event that was synchronous with deformation and associated with the development of a common, continentally-dipping foliation (see above; Vice *et al.,* 2020). This similarity in *P-T* conditions suggests these unit may have been together during the latter Buchan event experienced by the Kluane Schist. Equally, similarity in graphitic-rich protolith for both the Kluane Schist and Blanchard River assemblage (Bordet *et al*., 2015, Vice *et al*., 2020) along with their similar detrital zircon age spectra (Israel *et al.,* 2011a, Vice, 2017) suggest both units were likely sourced from similar, inboard continental regions.

Considering this, we suggest that the protolith for the Kluane Schist was likely deposited within a younger, but similarly positioned, depocenter to the Blanchard River assemblage (Fig. 1b). The deposition of the younger Kluane Schist protolith (*e.g.,* Israel *et al.,* 2011a) likely occurred coeval with the deeper-seated metamorphism experienced by the Blanchard River assemblage. This inference is supported by both the younger maximum depositional age suggested for the Kluane Schist (*ca.* 94 Ma; Israel *et al.,* 2011a) compared with the Blanchard River assemblage (*ca.* 120–130 Ma; Vice, 2017) and the lack of evidence for high-*P* burial metamorphism experienced by the Kluane Schist (our D_1M_1 above; Fig. 14). Combined, our results provide strong evidence against a direct correlation between the Kluane Schist and the Blanchard River assemblage. Instead, we suggest the Kluane Basin represents a younger depocenter of limited extent, which was open and receiving detritus during the very latter stages of Insular terrane accretion, with its lack of distinct high-pressure M_1 assemblages reflecting its significantly shallower underplating below the below the North American margin during Insular terrane accretion.

7. Conclusions

The Kluane Schist preserves an excellent example of a low-medium pressure, high temperature Buchan-style metamorphic field gradient. Our detailed revaluation of the metamorphic-deformational history experienced by the Kluane Schist suggests it experienced two distinct phases of metamorphism; an initial sub-greenschist-facies event, expressed through the development of S_1 bedding-parallel chlorite–calcite–titanite fabrics and a second more penetrative episode demonstrated through the progressive transposition of the lower grade S_1 foliation initially into a S_{2a} oblique chlorite–muscovite fabric and eventually to the pervasive, planar, biotite-rich S_{2b} foliation and centimetre-spaced, biotite–sillimanite–cordierite (+/- melt) gneissic fabric. Combined, these events are reflected as a metamorphic field gradient across the Kluane Schist. We document isograd continuity relating to this metamorphism across the Kluane Schist which is at odds with previous suggestions that it represents the juxtaposition of two distinct regionally metamorphosed tectonic belts. Further, the coupled metamorphic-deformational evolution we record across the Kluane Schist shows limited relationship to the Ruby Range Batholith and is not consistent with the presence of an ~5–6 km wide static contact aureole.

Instead, we view the Kluane Basin as a relativity young depocenter that was infilled during the very late stages of Insular terrane accretion. Metamorphism and deformation occurred during the waning stages of Insular terrane accretion when the Kluane Schist experienced limited tectonic burial below the North American margin followed by its wholesale underthrusting below a thermally mature Yukon-Tanana terrane. This process likely drove the pervasive Buchan-style metamorphism preserved across the Kluane Schist and developed the WNW- to W- directed non-coaxial structures observed at higher metamorphic grades. Later tops-to-the-SW shear structures, which overprint S_{2b} fabrics and dominate the inverted basin, likely developed in response to the SW-directed override of the Yukon-Tanana terrane. This transition was most likely initiated by the inception of orogen-parallel tectonics and dextral strike-slip faulting which dominate Cordilleran orogenic evolution post-dating *ca.* 60 Ma onward. As such the Kluane Basin is unlikely to be correlative with other Jura-Cretaceous basins that show evidence for deeper-seated metamorphism and significant underplating below North America during Insular terrane accretion, including the Blanchard River assemblage.

8. Funding and Acknowledgements

This work was supported by Natural Sciences and Engineering Research Council (NSERC) Discovery Grants awarded to HDG and BD. The authors are grateful to the Yukon Geological Survey for supporting fieldwork and providing helicopter time. Maurice Colpron and Steve Israel are thanked for their insightful discussions and accompanying early fieldwork. Alex Rea and Raj Aulakh are thanked for their assistance during fieldwork. Dave Pattison and Trevor

Waldien are thanked for their constructive reviews that helped to clarify and strengthen the arguments within this contribution.

9. References

Aranovich, L.Y. & Newton, R.C. (1999). Experimental determination of CO_2-H_2O activity-composition relations at 600–1000 C and 6–14 kbar by reversed decarbonation and dehydration reactions. *American Mineralogist*, 84(9), pp. 1319-1332. https://doi.org/10.2138/am-1999-0908

Bader, T., Franz, L., De Capitani, C. & Zhang, L. (2014). The effect of water activity on calculated phase equilibria and garnet isopleth thermobarometry of granulites, with particular reference to Tongbai (east-central China). *European Journal of Mineralogy*, 26(1), 5-23. https://doi.org/10.1127/0935-1221/2013/0025-2351

Beyssac, O., Goffé, B., Chopin, C. & Rouzaud, J.N. (2002). Raman spectra of carbonaceous material in metasediments: a new geothermometer. *Journal of Metamorphic Geology*, 20(9), pp. 859-871. https://doi.org/10.1046/j.1525-1314.2002.00408.x

Bishop, D.G. (1972). Progressive metamorphism from prehnite-pumpellyite to greenschist facies in the Dansey Pass area, Otago, New Zealand. *Geological Society of America Bulletin*, 83(11), pp. 3177-3198. https://doi.org/10.1130/0016-7606(1972)83[3177:PMFPTG]2.0.CO;2

Box, S.E., Karl, S.M., Jones, J.V., Bradley, D.C., Haeussler, P.J. & O'Sullivan, P.B., (2019). Detrital zircon geochronology along a structural transect across the Kahiltna assemblage in the western Alaska

Range: Implications for emplacement of the Alexander-Wrangellia-Peninsular terrane against North America. *Geosphere*, 15(6), pp.1774-1808. https://doi.org/10.1130/GES02060.1

Breton, N.L. & Thompson, A.B., (1988). Fluid-absent (dehydration) melting of biotite in metapelites in the early stages of crustal anatexis. *Contributions to Mineralogy and Petrology*, 99(2), pp.226-237. https://doi.org/10.1007/BF00371463

Brown, M., Averkin, Y.A., McLellan, E.L. & Sawyer, E.W., (1995). Melt segregation in migmatites. Journal of Geophysical Research: *Solid Earth*, 100(B8), pp. 15655-15679. https://doi.org/10.1029/95JB00517

Canil, D., Johnston, S.T., D'Souza, R.J. & Heaman, L.M., (2015). Protolith of ultramafic rocks in the Kluane Schist, Yukon, and implications for arc collisions in the northern Cordillera. *Canadian Journal of Earth Sciences*, 52(7), pp. 431-443. https://doi.org/10.1139/cjes-2014-0138

Chu, X. & Ague, J.J., (2013). Phase equilibria for graphitic metapelite including solution of CO2 in melt and cordierite: implications for dehydration, partial melting and graphite precipitation. *Journal of Metamorphic Geology*, 31(8), pp.843-862. https://doi.org/10.1111/jmg.12047

Coggon, R. & Holland, T.J.B., (2002). Mixing properties of phengitic micas and revised garnet-phengite thermobarometers. *Journal of Metamorphic Geology*, 20(7), pp.683-696. https://doi.org/10.1046/j.1525-1314.2002.00395.x

Colpron, M., Nelson, J.L., & Murphy, D.C. (2007). Northern Cordilleran terranes and their interactions through time. *GSA Today*, 17(4/5), xx. https://doi.org/10.1130/GSAT01704-5A.1

Colpron, M. and Nelson, J.L., (2011). A Digital Atlas of Terranes for the Northern Cordillera; *British Columbia Ministry of Energy and Mines*, BCGS GeoFile 2011-11.

Connolly J. A. & Bodnar R. J. (1983) A modified Redlich–Kwong equation of state for H2O–CO2 mixtures: application to fluid inclusion studies. *EOS 64*, (abstr.), pp. 350.

Coombs, D.S., Nakamura, Y. & Vuagnat, M., (1976). Pumpellyite-actinolite facies schists of the Taveyanne Formation near Loèche, Valais, Switzerland. *Journal of Petrology*, 17(4), pp.440-471. https://doi.org/10.1093/petrology/17.4.440

Davidson, C., Hollister, L.S. & Schmid, S.M., (1992). Role of melt in the formation of a deep-crustal compressive shear zone: The MaClaren Glacier metamorphic belt, south central Alaska. *Tectonics*, 11(2), pp.348-359. https://doi.org/10.1029/91TC02907

Davidson, C., & McPhillips, D., (2007), Along strike variations in metamorphism and deformation of the strata of the Kahiltna basin, south-central Alaska, in Ridgway, K.D., Trop, J.M., Glen, J.M.G., & O'Neill, J.M., eds., Tectonic growth of a collisional continental margin: crustal evolution of southern Alaska: Geological Society of America Special Paper 431, p. 439–454. https://doi.org/10.1130/2007.2431(17)

de Capitani, C. & Brown, T.H., (1987). The computation of chemical equilibrium in complex systems containing non-ideal solutions. *Geochimica et Cosmochimica Acta*, 51(10), pp.2639-2652. https://doi.org/10.1016/0016-7037(87)90145-1 de Capitani, C. & Petrakakis, K., (2010). The computation of equilibrium assemblage diagrams with Theriak/Domino software. *American mineralogist*, 95(7), pp.1006-101 https://doi.org/10.2138/am.2010.3354

Dempster, T.J., La Piazza, J., Taylor, A.G., Beaudoin, N. & Chung, P., (2017). Chemical and textural equilibration of garnet during amphibolite facies metamorphism: The influence of coupled dissolution–reprecipitation. *Journal of Metamorphic Geology*, 35(9), pp.1111-1130. https://doi.org/10.1111/jmg.12278

Dyck, B., Goddard, R.M., Wallis, D., Hansen, L.N. & Martel, E., (2021). Metamorphic evolution of the Great Slave Lake shear zone. *Journal of Metamorphic Geology*, 39(5), pp.567-590. https://doi.org/10.1111/jmg.12576

Eisbacher, G.H., (1976). Sedimentology of the Dezadeash flysch and its implications for strike-slip faulting along the Denali fault, Yukon Territory and Alaska. *Canadian Journal of Earth Sciences*, 13(11), pp.1495-1513. https://doi.org/10.1139/e76-157

Erdmer, P. & Mortensen, J.K., 1993. A 1200-km-long Eocene metamorphic-plutonic belt in the northwestern Cordillera: Evidence from southwest Yukon. *Geology*, 21(11), pp.1039-1042. https://doi.org/10.1130/0091-7613(1993)021<1039:AKLEMP>2.3.CO;2

Ernst, W.G., 1963. Significance of phengitic micas from low-grade schists. *American Mineralogist: Journal of Earth and Planetary Materials*, *48*(11-12), pp.1357-1373.

Forshaw, J.B., Pattison, D.R.M. Ferrous/ferric (Fe^{2+}/Fe^{3+}) partitioning among silicates in metapelites. *Contrib Mineral Petrol* **176**, 63 (2021). https://doi.org/10.1007/s00410-021-01814-4

Frezzotti, M.L., Tecce, F. & Casagli, A., (2012). Raman spectroscopy for fluid inclusion analysis. *Journal of Geochemical Exploration*, 112, pp.1-20. DOI: 10.1016/j.gexplo.2011.09.009

Gehrels, G.E., McClelland, W.C., Samson, S.D., Patchett, P.J. & Orchard, M.J., (1992). Geology of the western flank of the Coast Mountains between Cape Fanshaw and Taku Inlet, southeastern Alaska. *Tectonics*, 11(3), pp.567-585. https://doi.org/10.1029/92TC00482

Gehrels, G., Rusmore, M., Woodsworth, G., Crawford, M., Andronicos, C., Hollister, L., Patchett, J., Ducea, M., Butler, R., Klepeis, K. & Davidson, C., (2009). U-Th-Pb geochronology of the Coast Mountains batholith in north-coastal British Columbia: Constraints on age and tectonic evolution. *Geological Society of America Bulletin*, *121*(9-10), pp.1341-1361. https://doi.org/10.1130/B26404.1

Giorgetti, G., Frezzotti, M.L., Palmeri, R. & Burke, E.A.J., (1996). Role of fluids in migmatites: CO2-H2O fluid inclusions in leucosomes from the Deep Freeze Range migmatites (Terra Nova Bay, Antarctica). *Journal of Metamorphic Geology*, 14(3), pp.307-317. https://doi.org/10.1111/j.1525-1314.1996.00307.x

Guidotti, C.V. & Dyar, M.D., (1991). Ferric iron in metamorphic biotite and its petrologic and crystallochemical implications. *American Mineralogist*, 76(1-2), pp.161-175.

Holdaway, M.J., (2000). Application of new experimental and garnet Margules data to the garnet-biotite geothermometer. *American mineralogist*, 85(7-8), pp.881-892. https://doi.org/10.2138/am-2000-0701

Hart, C.J., Goldfarb, R.J., Lewis, L.L. & Mair, J.L., (2004). The Northern Cordilleran Mid-Cretaceous plutonic province: Ilmenite/magnetite-series granitoids and intrusion-related mineralisation. *Resource Geology*, *54*(3), pp.253-280. https://doi.org/10.1111/j.1751-3928.2004.tb00206.x

Holland, T.J.B. & Powell, R.T.J.B., 1998. An internally consistent thermodynamic data set for phases of petrological interest. *Journal of metamorphic Geology*, 16(3), pp.309-343. https://doi.org/10.1111/j.1525-1314.1998.00140.x

Holland, T. & Powell, R., (2003). Activity–composition relations for phases in petrological calculations: an asymmetric multicomponent formulation. *Contributions to Mineralogy and Petrology*, 145(4), pp.492-501. https://doi.org/10.1007/s00410-003-0464-z

Holland, T.J.B. & Powell, R., (2009). AX: A program to calculate activities of mineral end members from chemical analysis. *Retrieved from:*https://filedn.com/lU1GlyFhv3UuXg5E9fbnWFF/TJBHpages/ax.html. Last updated, October 2019.

Holland, T.J.B. & Powell, R., (2011). An improved and extended internally consistent thermodynamic dataset for phases of petrological interest, involving a new equation of state for solids. *Journal of metamorphic Geology*, 29(3), pp.333-383. https://doi.org/10.1111/j.1525-1314.2010.00923.x

Hults, C.P., Wilson, F.H., Donelick, R.A. & O'Sullivan, P.B., (2013). Two flysch belts having distinctly different provenance suggest no stratigraphic link between the Wrangellia composite terrane and the paleo-Alaskan margin. *Lithosphere*, 5(6), pp.575-594. https://doi.org/10.1130/L310.1

Israel, S., Murphy, D., Bennett, V., Mortensen, J. and Crowley, J., 2011a. New insights into the geology and mineral potential of the Coast Belt in southwestern Yukon. In: Yukon Exploration and Geology 2010, MacFarlane, K.E., Weston, L.H., and Relf, C. (eds.), *Yukon Geological Survey*, p. 101-123.

Israel, S., Cobbett, R., Westberg, E., Stanley, B. & Hayward, N., 2011b. Preliminary bedrock geology of the Ruby Ranges, southwestern Yukon, (Parts of NTS 115G, 115H, 115A and 115B) (1:150 000 scale). *Yukon Geological Survey*, Open File 2011-2.

Israel, S., Colpron, M., Cubley, J., Moynihan, D., Murphy, D.C. & Relf, C., (2015). The Bear Creek assemblage: A latest Triassic volcano-sedimentary succession in southwest Yukon. In: Yukon Exploration and Geology 2014, K.E. MacFarlane, M.G. Nordling and P.J. Sack (eds.), *Yukon Geological Survey*, p. 99-112.

Kent, D.V. & Irving, E., (2010). Influence of inclination error in sedimentary rocks on the Triassic and Jurassic apparent pole wander path for North America and implications for Cordilleran tectonics. *Journal of Geophysical Research: Solid Earth*, 115(B10). https://doi.org/10.1029/2009JB007205

Kohn, M.J. and Spear, F., 2000. Retrograde net transfer reaction insurance for pressure-temperature estimates. *Geology*, *28*(12), pp.1127-1130. https://doi.org/10.1130/0091-7613(2000)28<1127:RNTRIF>2.0.CO;2

Kohn, M. J. (2014). Geochemical zoning in metamorphic minerals. Treatise on Geochemistry, 4, 249-280. https://doi.org/10.1016/B0-08-043751-6/03176-5

Lamadrid, H.M., Moore, L.R., Moncada, D., Rimstidt, J.D., Burruss, R.C. & Bodnar, R.J., (2017). Reassessment of the Raman CO2 densimeter. *Chemical Geology*, 450, pp.210-222. http://dx.doi.org/10.1016/j.chemgeo.2016.12.034

Lamb, W.M. & Valley, J.W., (1988). Granulite facies amphibole and biotite equilibria, and calculated peak-metamorphic water activities. *Contributions to Mineralogy and Petrology*, 100(3), pp.349-360. https://doi.org/10.1007/BF00379744

Law, R.D., (1986). Relationships between strain and quartz crystallographic fabrics in the Roche Maurice quartzites of Plougastel, western Brittany. *Journal of Structural Geology*, 8(5), pp.493-515. https://doi.org/10.1016/0191-8141(86)90001-5

Lowey, G.W., (2018). Provenance analysis of the Dezadeash Formation (Jurassic–Cretaceous), Yukon, Canada: Implications regarding a linkage between the Wrangellia composite terrane and the western margin of Laurasia. *Canadian Journal of Earth Sciences*, 56(1), pp.77-100. https://doi.org/10.1139/cjes-2017-0244

McClelland, W.C., Gehrels, G.E. & Saleeby, J.B., (1992). Upper Jurassic-Lower Cretaceous basinal strata along the Cordilleran margin: Implications for the accretionary history of the Alexander-Wrangellia-Peninsular terrane. *Tectonics*, 11(4), pp.823-835. https://doi.org/10.1029/92TC00241

Mehnert, K. R., (1968). Migmatites and the Origin of Granitic Rocks. x 393 p., 138 figs. Elsevier Publishing Company, Amsterdam, London, New York. Geological Magazine. *Cambridge University Press*, 106(2), pp. 222–223. doi: 10.1017/S0016756800052092.

Mezger, J.E., 1997. Tectonometamorphic evolution of the Kluane metamorphic assemblage, southwest Yukon: evidence for Late Cretaceous eastward subduction of oceanic crust underneath North America. *Unpublished PhD thesis*, University of Alberta, 306 p. https://doi.org/10.7939/R3DJ58N76

Mezger, J.E., (2010). Rotation of irregular staurolite porphyroblasts in a simple shear dominated shear zone controlled by initial growth orientation and aspect ratio. *Journal of Structural Geology*, 32(8), pp.1147-1157. https://doi.org/10.1016/j.jsg.2010.07.002

Mezger, J.E., 2000. 'Alpine-type' ultramafic rocks of the Kluane metamorphic assemblage, southwest Yukon: Oceanic crust fragments of a late Mesozoic back-arc basin along the northern Coast Belt. *In: Yukon Exploration and Geology 1999*, Emond, D.S. and Weston, L.W. (eds.), Exploration and Geological Sciences Division, Yukon Region, Indian and Northern Affairs Canada, pp. 127-138.

Mezger, J.E., Chacko, T. & Erdmer, P., (2001). Metamorphism at a late Mesozoic accretionary margin: a study from the Coast Belt of the North American Cordillera. Journal of Metamorphic Geology, 19(2), pp.121-137. https://doi.org/10.1046/j.0263-4929.2000.00300.x

Monger, J.W., (2014). Logan Medallist 1. Seeking the suture: The Coast-Cascade conundrum. *Geoscience Canada,* 41(4), pp.379-398. https://doi.org/10.12789/geocanj.2014.41.058

Monger, J.W. & Gibson, H.D., (2019). Mesozoic-Cenozoic deformation in the Canadian Cordillera: The record of a “Continental bulldozer”?. *Tectonophysics*, 757, pp.153-169. https://doi.org/10.1016/j.tecto.2018.12.023

Monger, J.W.H., Price, R.A., & Tempelman-Kluit, D.J., (1982), Tectonic accretion and the origin of the two major metamorphic and tectonic welts in the Canadian Cordillera. *Geology*, 10(2), 70–75. https://doi.org/10.1130/0091-7613(1982)10<70:TAATOO>2.0.CO;2

Monger, J.W.H., Van der Heyden, P., Journeay, J.M., Evenchick, C.A. & Mahoney, J.B., (1994). Jurassic-Cretaceous basins along the Canadian Coast Belt: Their bearing on pre-mid-Cretaceous sinistral displacements. *Geology*, 22(2), pp.175-178. https://doi.org/10.1130/0091-7613(1994)022<0175:JCBATC>2.3.CO;2

Mukherjee, S., (2017). Review on symmetric structures in ductile shear zones. International Journal of Earth Sciences, 106(5), pp.1453-1468. DOI: 10.1007/s00531-016-1366-4

Nelson, J. L., Colpron, M. & Israel, S. (2013). The cordillera of British Columbia, Yukon, and Alaska. *Society of Economic Geology*, 2013, Special Publication 17. https://doi.org/10.5382/SP.17.03

Nokleberg, W.J., Jones, D.L. & Silberling, N.J., (1985). Origin and tectonic evolution of the Maclaren and Wrangellia terranes, eastern Alaska Range, Alaska. *Geological Society of America Bulletin*, 96(10), pp.1251-1270. https://doi.org/10.1130/0016-7606(1985)96<1251:OATEOT>2.0.CO;2

Pattison, D.R. & Goldsmith, S.A., (2022). Metamorphism of the Buchan type-area, NE Scotland and its relation to the adjacent Barrovian domain. *Journal of the Geological Society*, 179(1). https://doi.org/10.1144/jgs2021-0

Pattison, D.R.M. & DeBuhr, C.L., (2015). Petrology of metapelites in the Bugaboo aureole, British Columbia, Canada. *Journal of Metamorphic Geology*, 33(5), pp.437-462. https://doi.org/10.1111/jmg.12128

Phillips, G.N., (1981). Water activity changes across an amphibolite-granulite facies transition, Broken Hill, Australia. *Contributions to Mineralogy and Petrology*, 75(4), pp.377-386. DOI: 0010-7999/80/0075/0377/.

Powell, R. & Holland, T., (1994). Optimal geothermometry and geobarometry. *American Mineralogist*, 79(1-2), pp.120-133. DOI: 0003-004X/94/0102-0120.

Powell, R. & Holland, T.J.B., (2008). On thermobarometry. *Journal of Metamorphic Geology*, 26(2), pp.155-179. https://doi.org/10.1111/j.1525-1314.2007.00756.x

Ramsay, C.R. The origin of biotite in Archaean meta-sediments near Yellowknife, N. W. T., Canada. *Contr. Mineral. and Petrol.* **42**, 43–54 (1973). https://doi.org/10.1007/BF00521646

Redler, C., White, R.W. & Johnson, T.E., (2013). Migmatites in the Ivrea Zone (NW Italy): Constraints on partial melting and melt loss in metasedimentary rocks from Val Strona di Omegna. *Lithos*, 175, pp.40-53. https://doi.org/10.1016/j.lithos.2013.04.019

Sawyer, E.W., Dombrowski, C. & Collins, W.J., (1999). Movement of melt during synchronous regional deformation and granulite-facies anatexis, an example from the Wuluma Hills, central Australia. *Geological Society, London, Special Publications*, 168(1), pp.221-237. https://doi.org/10.1144/GSL.SP.1999.168.01.15

Sigloch, K. & Mihalynuk, M.G., (2013). Intra-oceanic subduction shaped the assembly of Cordilleran North America. *Nature*, 496(7443), pp.50-56. https://doi.org/10.1038/nature12019

Sigloch, K. & Mihalynuk, M.G., (2017). Mantle and geological evidence for a Late Jurassic–Cretaceous suture spanning North America. *GSA Bulletin*, 129(11-12), pp.1489-1520. https://doi.org/10.1130/B31529.1

Smith, T.E., (1981), Geology of the Clearwater Mountains, south-central Alaska. *Alaska Division of Geological & Geophysical Surveys Geologic Report 60*, pp. 72, 3 sheets, scale 1:63,360. https://doi.org/10.14509/406

Spear, F.S. & Cheney, J.T., (1989). A petrogenetic grid for pelitic schists in the system SiO2-Al2O3-FeO-MgO-K2O-H2O. *Contributions to Mineralogy and Petrology*, 101(2), pp.149-164. https://doi.org/10.1007/BF00375302

Spear, F.S., (1993). Metamorphic phase equilibria and pressure–temperature–time paths. *Mineralogical Society of America Monograph*, Washington, D.C., pp. 1-799.

Spry, A., (1974). Metamorphic textures. *Pergamon Press*, Oxford, pp. 240–246

Stanley, B., (2012). Structural geology and geochronology of the Kluane schist, southwestern Yukon Territory. *UWSpace. http://hdl.handle.net/10012/7096* (unpublished Master's thesis, University of Waterloo).

Steele-MacInnis, M., (2018). Fluid inclusions in the system H2O-NaCl-CO2: An algorithm to determine composition, density and isochore. *Chemical Geology*, 498, pp.31-44. https://doi.org/10.1016/j.chemgeo.2018.08.022

St-Onge, M.R. & Davis, W.J., (2018). Wopmay orogen revisited: Phase equilibria modeling, detrital zircon geochronology, and U-Pb monazite dating of a regional Buchan-type metamorphic sequence. *GSA Bulletin*, 130(3-4), pp.678-704. https://doi.org/10.1130/B31809.1

Sugisaki, R., (1984). Relation between chemical composition and sedimentation rate of Pacific ocean-floor sediments deposited since the middle Cretaceous: basic evidence for chemical constraints on depositional environments of ancient sediments. *The Journal of Geology*, 92(3), pp.235-259. https://doi.org/10.1086/628858

Sun, Q., Zhao, L., Li, N., Liu, J., (2010). Raman spectroscopic study for the determination of Cl− concentration (molarity scale) in aqueous solutions: Application to fluid inclusions. *Chemical Geology*, 272(1-4), pp. 55-61. https://doi.org/10.1016/j.chemgeo.2010.02.004

Tempelman-Kluit, D. J., (1974). Reconnaissance geology of Aishihik Lake, Snag and part of Stewart River map-areas, west-central Yukon; Tempelman-Kluit, D J. Geological Survey of Canada, Paper 73-41, 1974, 97 pages (3 sheets), https://doi.org/10.4095/102542

Thompson Jr, J.B., (1957). The graphical analysis of mineral assemblages in pelitic schists. *American Mineralogist: Journal of Earth and Planetary Materials*, 42(11-12), pp.842-858.

Utada, M., (2001). Zeolites in hydrothermally altered rocks. *Reviews in mineralogy and geochemistry*, 45(1), pp. 305-322. https://doi.org/10.2138/rmg.2001.45.10

van der Heyden, P., (1992). A Middle Jurassic to early Tertiary Andean-Sierran arc model for the Coast belt of British Columbia. *Tectonics*, 11(1), pp.82-97. https://doi.org/10.1029/91TC02183

Vice, L., Gibson, H. D. &Israel, S., (2020). Late Cretaceous to Paleocene Tectonometamorphic Evolution of the Blanchard River Assemblage, Southwest Yukon: New Insight into the Terminal Accretion of Insular Terranes in the Northern Cordillera. *Lithosphere*, 2020(1): 2298288. https://doi.org/10.2113/2020/2298288

Waldien, T.S., Roeske, S.M., Benowitz, J.A., Twelker, E. & Miller, M.S., (2021a). Oligocene-Neogene lithospheric-scale reactivation of Mesozoic terrane accretionary structures in the Alaska Range suture zone, southern Alaska, USA. *GSA Bulletin*, 133(3-4), pp.691-716. https://doi.org/10.1130/B35665.1

Waldien, T.S., Roeske, S.M. & Benowitz, J.A., (2021b). Tectonic underplating and dismemberment of the Maclaren-Kluane schist records Late Cretaceous terrane accretion polarity and ~480 km of Post-52 Ma dextral displacement on the Denali Fault. *Tectonics*, 40(10), e2020TC006677. https://doi.org/10.1029/2020TC006677

Waters, D. J., (1988), Partial melting and the formation of granulite facies assemblages in Namaqualand, South Africa: *Journal of Metamorphic Geology*, v. 6, pp. 387–404. https://doi.org/10.1111/j.1525-1314.1988.tb00430.x

Waters, D.J., (2019). Metamorphic constraints on the tectonic evolution of the High Himalaya in Nepal: the art of the possible. *Geological Society, London, Special Publications*, 483(1), pp.325-375. https://doi.org/10.1144/SP483-2018-187

White, R.W., Powell, R. & Clarke, G.L., (2002). The interpretation of reaction textures in Fe-rich metapelitic granulites of the Musgrave Block, central Australia: constraints from mineral equilibria calculations in the system K2O–FeO–MgO–Al2O3–SiO2–H2O–TiO2–Fe2O3. *Journal of metamorphic Geology*, 20(1), pp.41-55. https://doi.org/10.1046/j.0263-4929.2001.00349.x

White, R.W., Powell, R. & Holland, T.J.B., (2001). Calculation of partial melting equilibria in the system Na2O–CaO–K2O–FeO–MgO–Al2O3–SiO2–H2O (NCKFMASH). *Journal of metamorphic Geology*, 19(2), pp.139-153. https://doi.org/10.1046/j.0263-4929.2000.00303.x

White, R.W., Powell, R. & Holland, T.J.B., (2007). Progress relating to calculation of partial melting equilibria for metapelites. *Journal of metamorphic Geology*, 25(5), pp.511-527. https://doi.org/10.1111/j.1525-1314.2007.00711.x

White, R.W., Powell, R.O.G.E.R., Holland, T.J.B., Johnson, T.E. & Green, E.C.R., (2014). New mineral activity–composition relations for thermodynamic calculations in metapelitic systems. *Journal of Metamorphic Geology*, 32(3), pp.261-286. https://doi.org/10.1111/jmg.12071

Whitney, D.L. & Evans, B.W., (2010). Abbreviations for names of rock-forming minerals. *American mineralogist*, 95(1), pp.185-187. https://doi.org/10.2138/am.2010.3371

Will, T.M., Okrusch, M. & Gruner, B.B., (2004). Barrovian and Buchan type metamorphism in the Pan-African Kaoko belt, Namibia: implications for its geotectonic position within the framework of Western Gondwana. *South African Journal of Geology*, 107(3), pp.431-454. https://doi.org/10.2113/107.3.431

Wu, C.M., (2015). Revised empirical garnet–biotite–muscovite–plagioclase geobarometer in metapelites. *Journal of Metamorphic Geology*, 33(2), pp.167-176. https://doi.org/10.1111/jmg.12115

Wu, C.M., (2017). Calibration of the garnet–biotite–Al2SiO5–quartz geobarometer for metapelites. *Journal of Metamorphic geology*, 35(9), pp.983-998. https://doi.org/10.1111/jmg.12264

Zwart, H.J., (1962). On the determination of polymetamorphic mineral associations, and its application to the Bosost area (Central Pyrenees). *Geologische Rundschau*, 52(1), pp.38-65. https://doi.org/10.1007/BF01840064

Figure Captions:

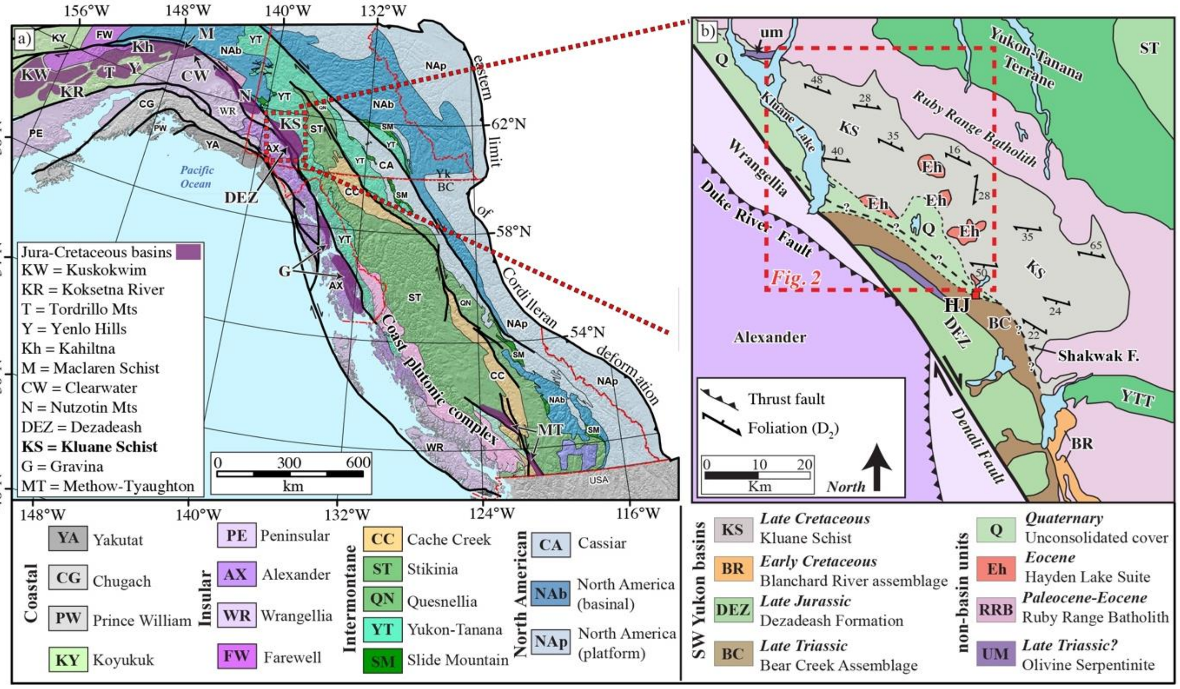

Figure 1. a) The location of the study area within the terrane collage of the Northern Canadian and Alaskan Cordillera (modified from Colpron & Nelson, 2011). The Jura-Cretaceous basinal assemblages that are situated between the Insular and Intermontane terranes, which includes the Kluane Schist, are highlighted and labelled. b) Map of the Kluane Basin, outlined by the red rectangle in (a). The distribution of the major lithologies within the Kluane Basin and their relationships to surrounding geological belts is shown (based on Mezger, 1997; Mezger *et al.,* 2001; Israel *et al.,* 2015; Vice *et al.,* 2020; this study).

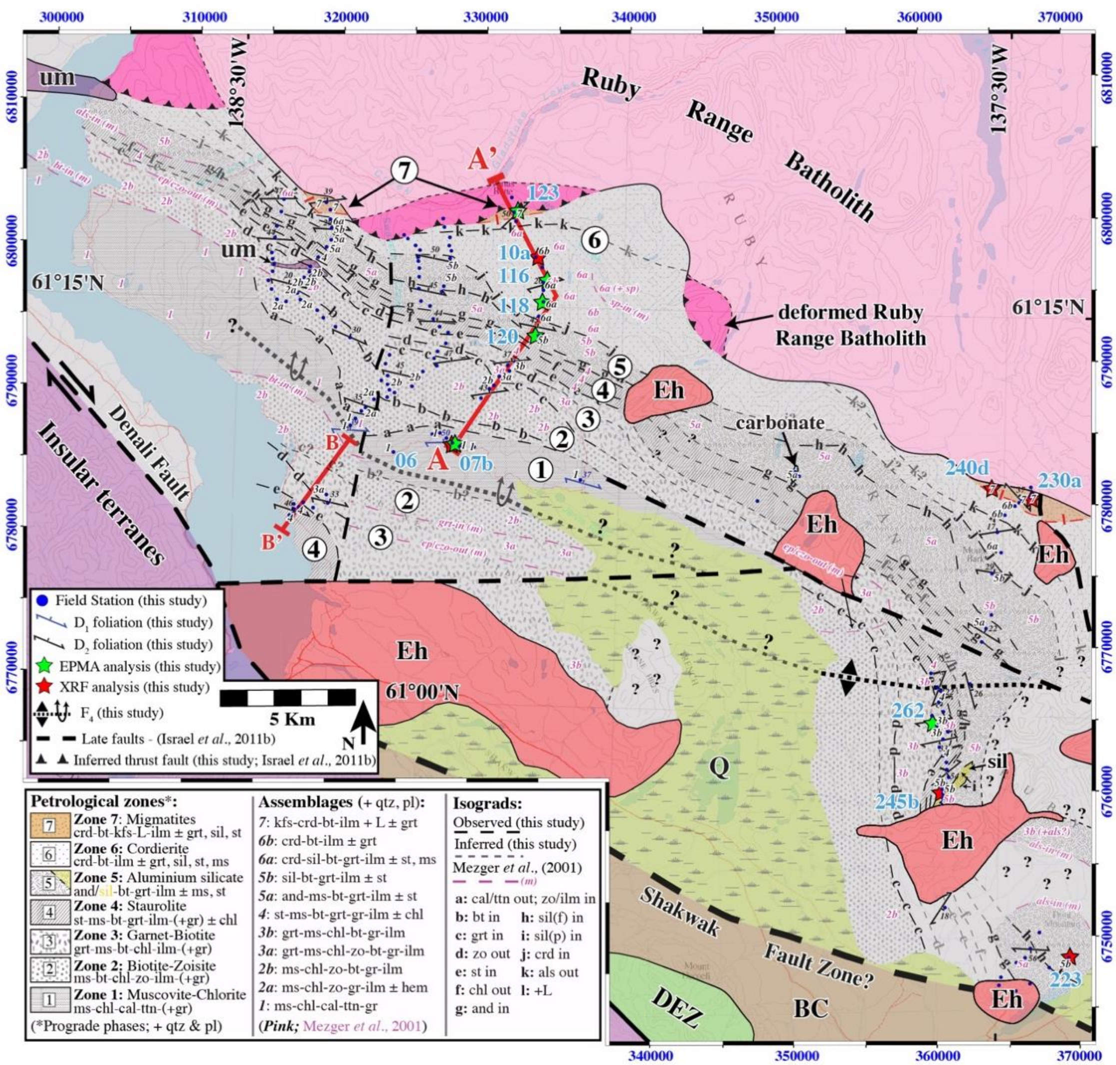

Figure 2. Assemblage map of northwest Kluane Basin (red rectangle in figure 1b; map based on Israel *et al.,* 2011b; Colpron & Neslon, 2011; Israel *et al.,* 2015; this study) outlining the petrological zones defined in this study. Lithologies are the same colour as in figure 1 except where indicated (*i.e.,* "deformed Ruby Range Batholith" & "carbonate"). Isograd locations are constrained by assemblage observations from this and previous studies (Mezger *et al.,* 2001). Petrological zones are highlighted by different shading patterns and indicated by circled numbers. Orange shading represents areas where leucosome is observed in Kluane Schist outcrops. Yellow shading highlights areas where prismatic sillimanite (labelled 'sil' on map and sil(p) in key) was

observed. The location of young faults was inferred from aeromagnetic surveys (Israel *et al.,* 2011b). Red stars represent samples taken for XRF analysis and green stars show samples taken for detailed EPMA analysis. Blue numbers refer to analysed samples.

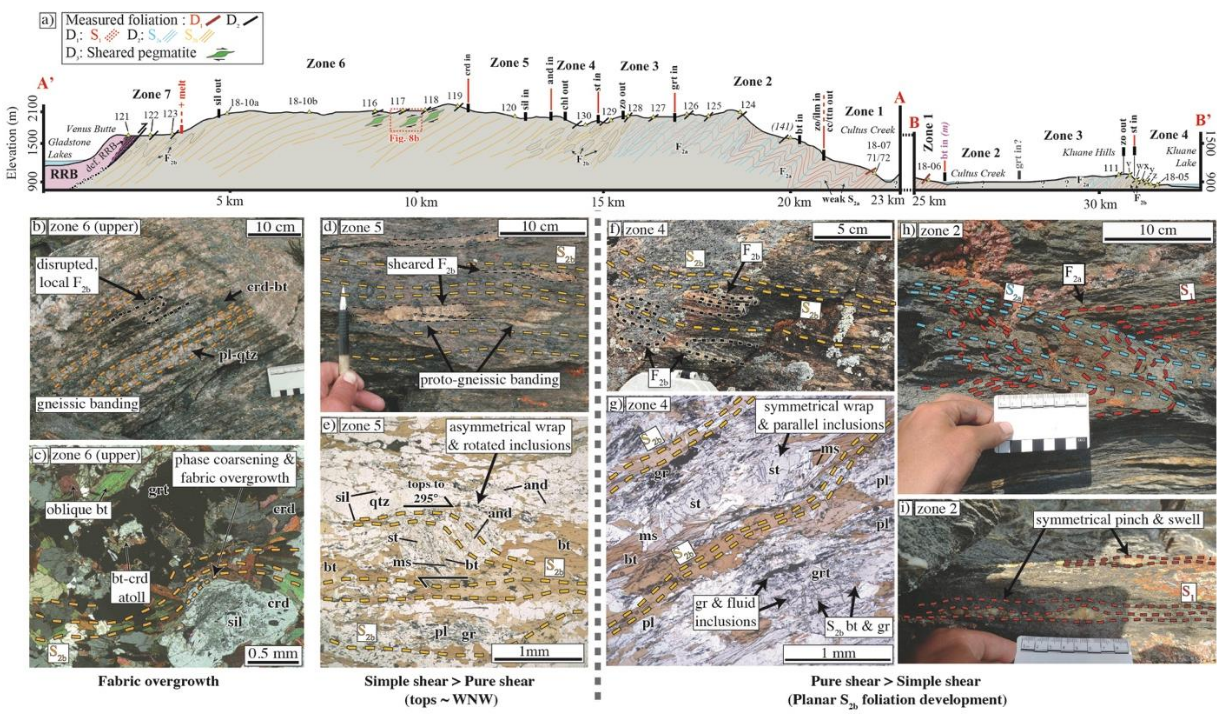

Figure 3. a) Cross section for lines A-A' and B-B' in figure 2 highlighting the relationship between petrologic zone and structural level across the Kluane Schist. Field stations are labelled and highlighted by yellow triangles (In B-B': v = 110; w = 109; x = 108; y = 106; z: 105/20-40). Average foliation measurements are indicated by short solid lines (Red = D_1, black = D_2). Bracketed and italic sample numbers (*e.g., 141*) represent measurements and observations that are projected onto the line of section from nearby localities. Observed fabrics and fold geometries (D_2) are projected into the subsurface. The sense-of-shear recorded by pegmatites (D_3), where observed, is also indicated. Isograds are directly labelled and indicated by thick solid lines. Photos (b–i)

document the typical structures and index minerals characteristic to each petrologic zone and are discussed in detail in the main text.

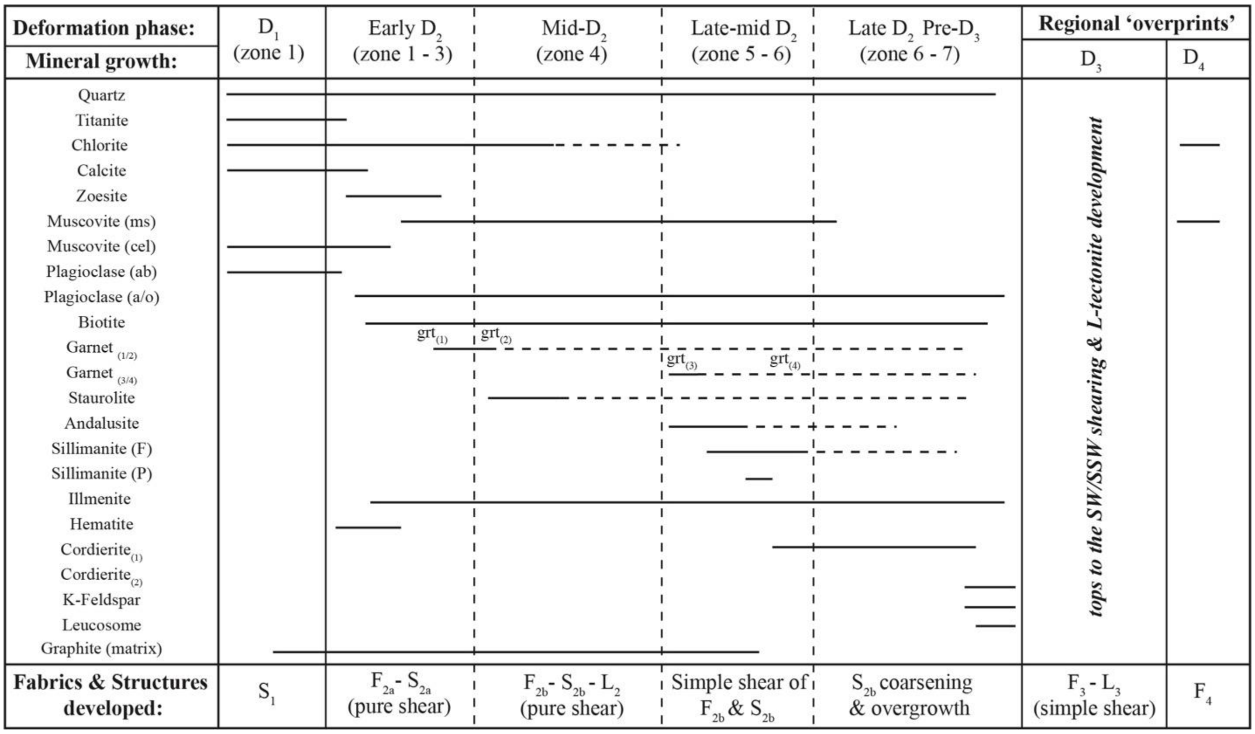

Figure 4. Box plot summarising the stability of different minerals with distinct deformation events and petrologic zones across the Kluane Schist. Solid lines show when each mineral is stable, dashed lines represent metastable mineral preservation. Ms = muscovite; cel = celadonite; ab = albite; a/o = andesine/oligoclase; Sillimanite (F) = fibrolitic sillimanite; Sillimanite (P) = prismatic sillimanite; grt(x) = garnet population x (see main text). Graphite stability refers to just that within the matrix, not porphyroblasts.

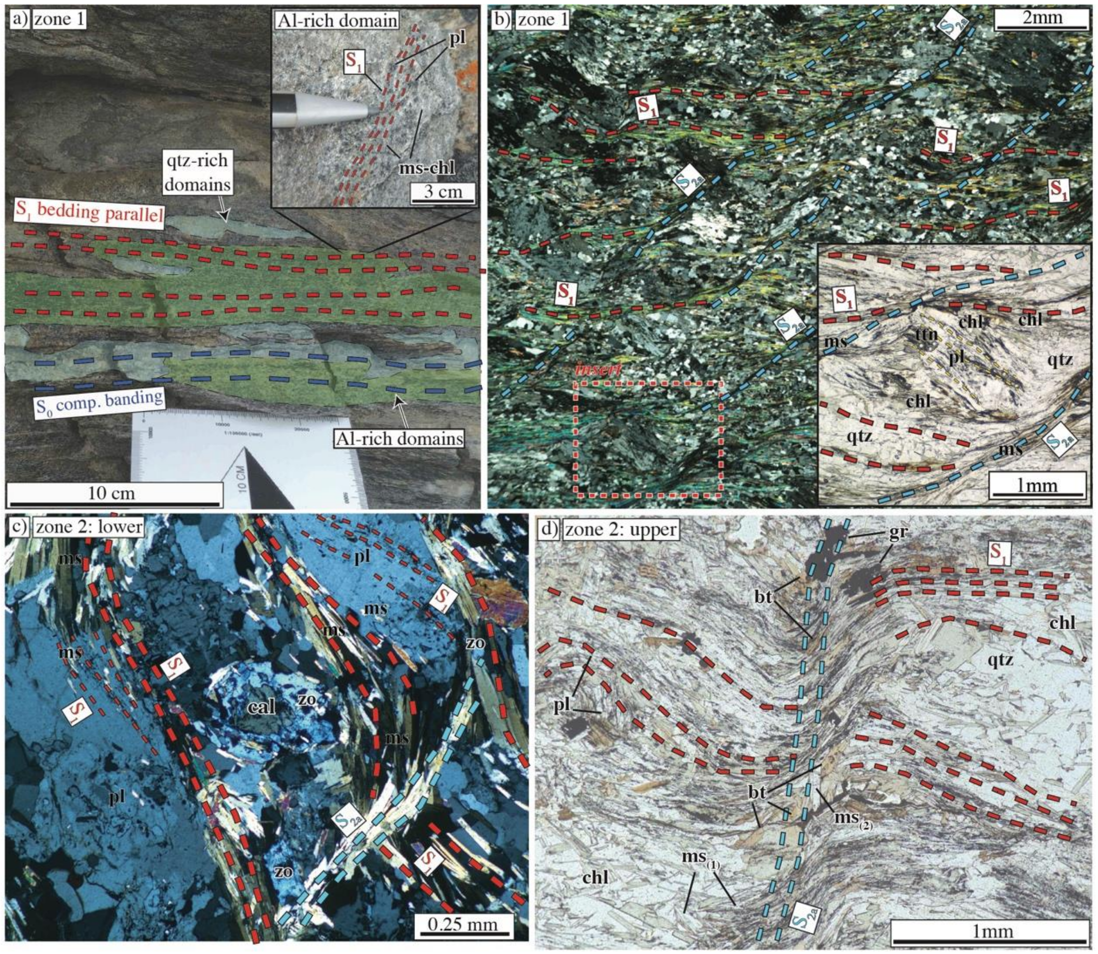

Figure 5. Outcrop photos and photomicrographs from zones 1 and 2. a) Muscovite-rich schist, typical of zone 1 towards the centre of the Kluane Basin (07b and 06 in Fig. 2). Centimetre-scale dark and light compositional bands (blue and green highlight) reflect original bedding (S_0). Insert shows muscovite–chlorite S_1 fabric overgrown by plagioclase porphyroblasts. b) Photomicrograph of zone 1 schist showing the relationship between fabrics and chlorite–muscovite–titanite assemblage. Note: inclusion trails in plagioclase (yellow dashed lines in insert) are oblique to matrix fabrics. c) Photomicrograph of a lower-grade sample within zone 2; the muscovite–chlorite S_1 fabric is overgrown by plagioclase and the muscovite-rich S_{2a} fabric. S_{2a} wraps zoisite and plagioclase. Calcite is observed as rare inclusions to zoisite. d) Photomicrograph of a higher-grade

zone 2 sample. Biotite is associated with a second generation of muscovite $ms_{(2)}$, with both primarily occurring in S_{2a} orientations.

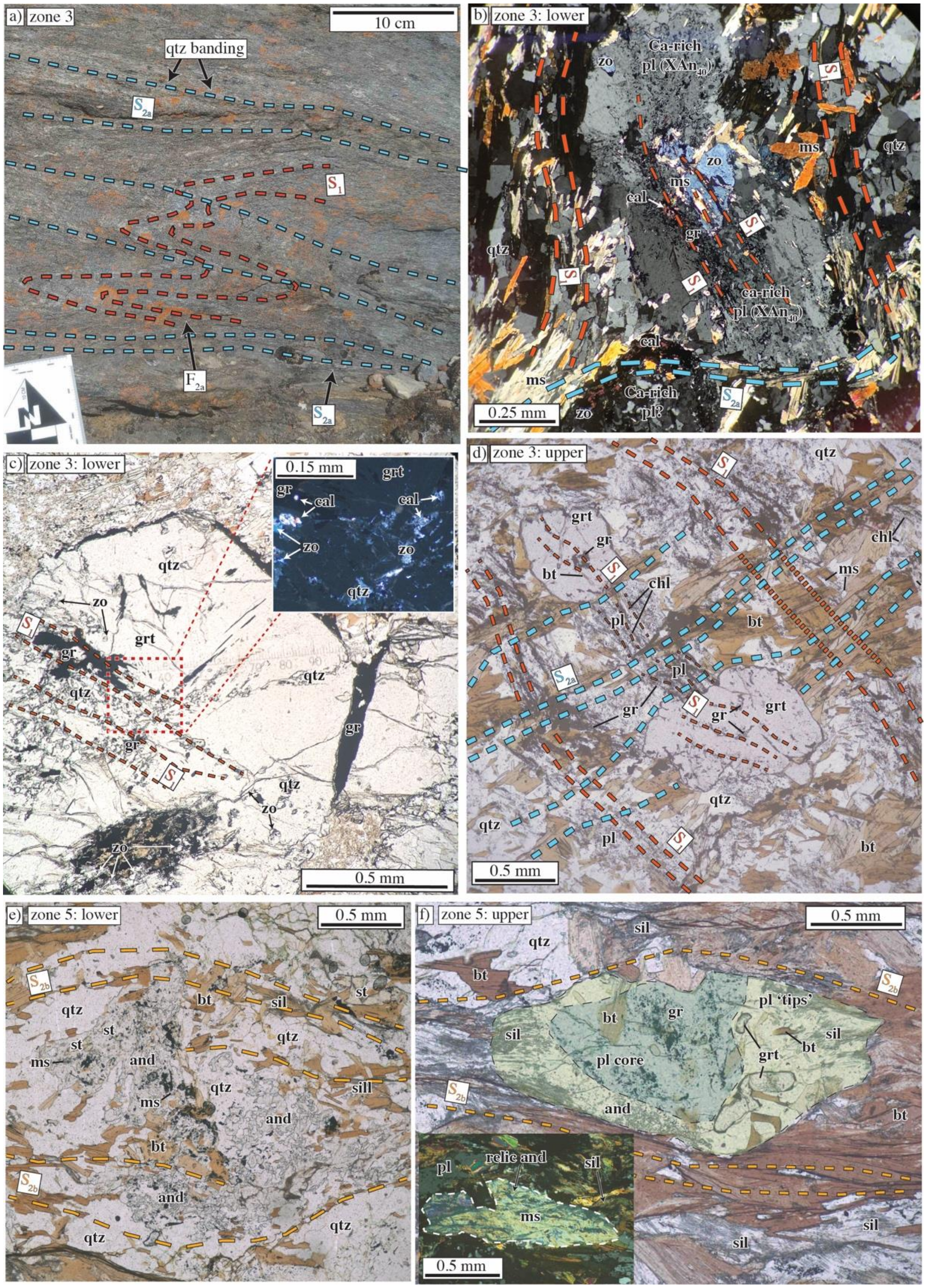

Figure 6. a) Outcrop photo of a zone 3 schist showing tight F_{2a} folds which are reclined and axial planar to a strong S_{2a} fabric. b) Photomicrograph of plagioclase typical of the lowest-grades units

of zone 3. Ca-rich plagioclase cores include zoisite and calcite, overgrow S_1 and are wrapped by S_{2a}. c) Photomicrograph of garnet typical of the lowest-grades units of zone 3. Garnet is coarse, well-faceted and hosts inclusions of calcite, zoisite and S_1 aligned graphite and quartz. d) Photomicrograph of a higher-grade zone 3 schist. Coarse euhedral garnet hosts S_1 aligned inclusions and is partially wrapped by a strong biotite-rich S_{2a} which overprints the relic chlorite–graphite S_1. e) Photomicrograph of a lower-grade zone 5 sample, knotty andalusite poikiloblasts are intergrown with quartz and the S_{2b} fabric and host inclusions of muscovite, biotite and staurolite. Staurolite remains as the dominant porphyroblast within this sample. f) In higher grade zone 5 assemblages fibrolitic sillimanite is associated with biotite-rich fabrics. Note: plagioclase shows distinct tips which are elongate into S_{2b} fabric orientations and host inclusions of andalusite, fibrolitic sillimanite and inclusion-free garnet. Insert shows a relic andalusite porphyroblast wrapped by biotite-rich S_{2b} and replaced by muscovite.

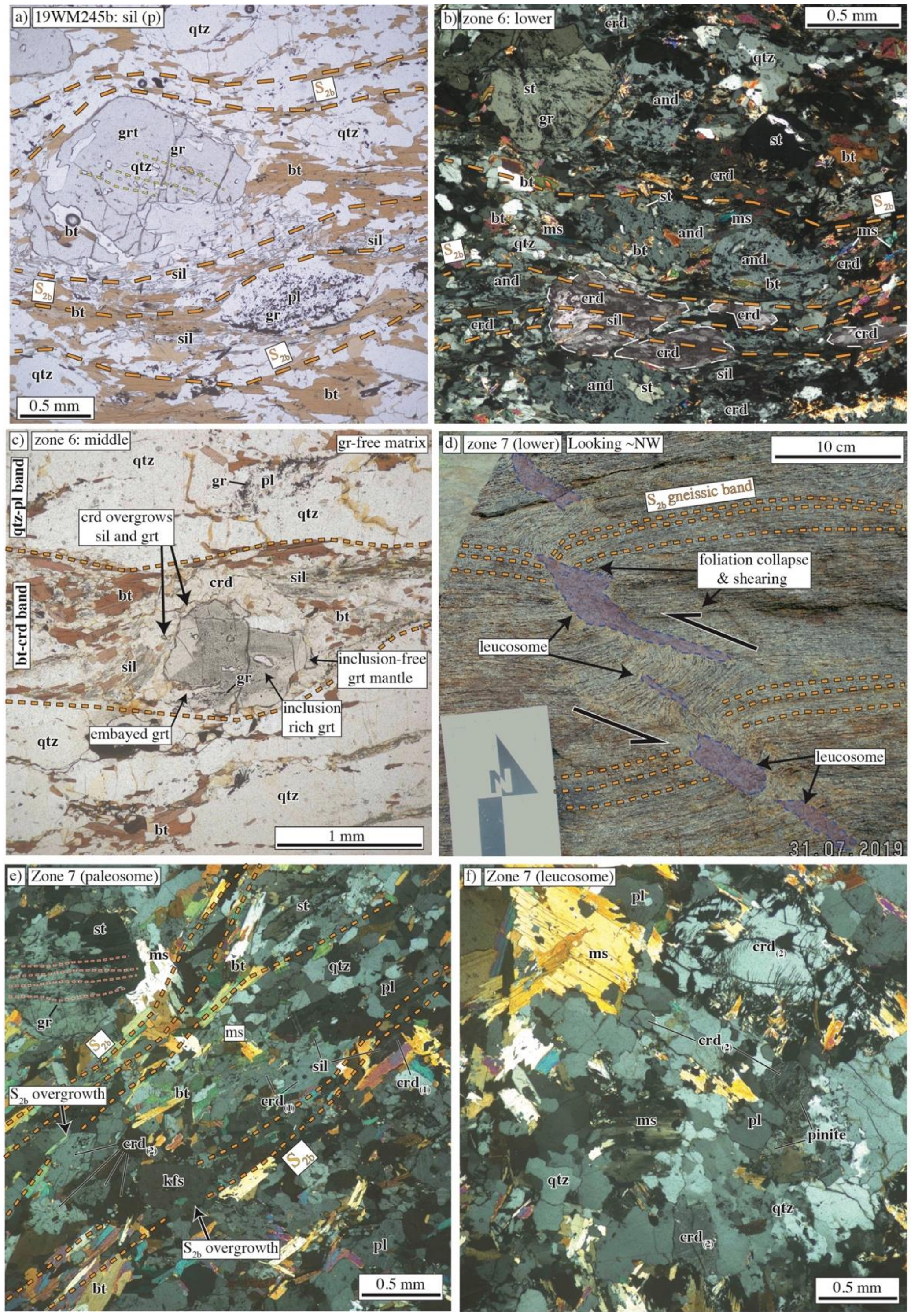

Figure 7. a) Photomicrograph of sample 19WM245b (245b in Fig. 2) highlighting the occurrence of prismatic sillimanite within staurolite-free zone 5 assemblages. Sillimanite tracks the biotite-

rich S_{2b} fabric and wraps inclusion-poor garnet. Oriented garnet inclusion trails are highlighted by yellow dashed lines. b) Photomicrograph showing the assemblage common to the lower-grade units of zone 6; cordierite occurs within, and aligned with, the biotite–muscovite–sillimanite S_{2b} fabric. Andalusite and staurolite occur as largely uncorroded porphyroblasts. c) Photomicrograph of a typical zone 6 assemblage. Cordierite replaces sillimanite and garnet and is entrained within the S_{2b} gneissic fabric. d) Outcrop photo of polymineralic leucosome lenses apparent within the lower grade regions of zone 7. The aligned lenses of leucosome appear to result from sinistral shearing and foliation collapse. e) Photomicrograph of paleosome domains within a zone 7 gneiss. K-feldspar, cordierite and muscovite overgrow a biotite-rich S_{2b} fabric. Note: two generations of cordierite; $crd_{(1)}$ is aligned with the S_{2b} fabric and hosts sillimanite inclusions while $crd_{(2)}$ overgrows S_{2b} and lacks sillimanite inclusions. f) Photomicrograph of the leucosome within zone 7. Retrograde muscovite overgrew these phases in random orientations.

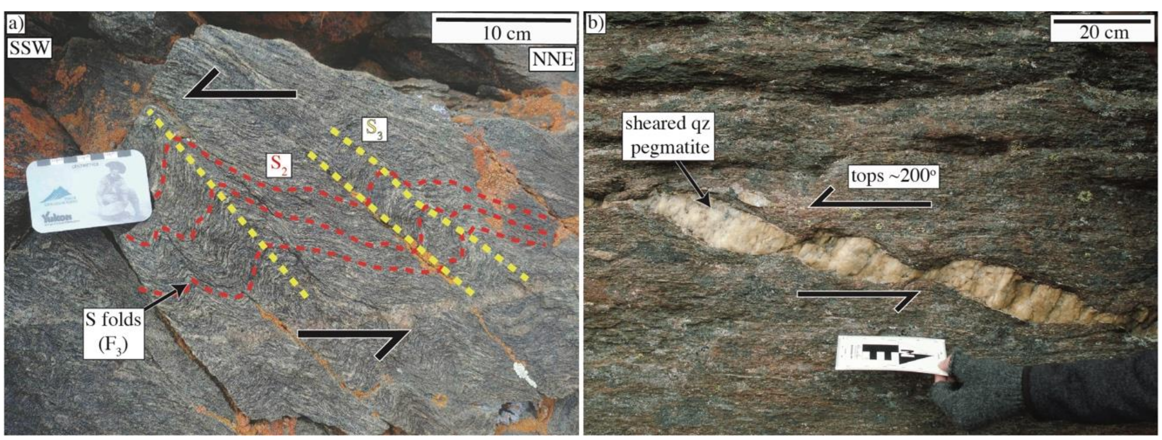

Figure 8. Later stage non-coaxial deformation (D_3) across the Kluane Schist. a) Asymmetric shear folds, F_3. Red dashed lines highlight the form of F_3 and yellow dashed lines the axial traces with

vergence towards the SSW. b) Coarse lensoidal quartz veins within a zone 6 outcrop that provide a tops-to-the-SW sense of shear (also see Fig. 3a).

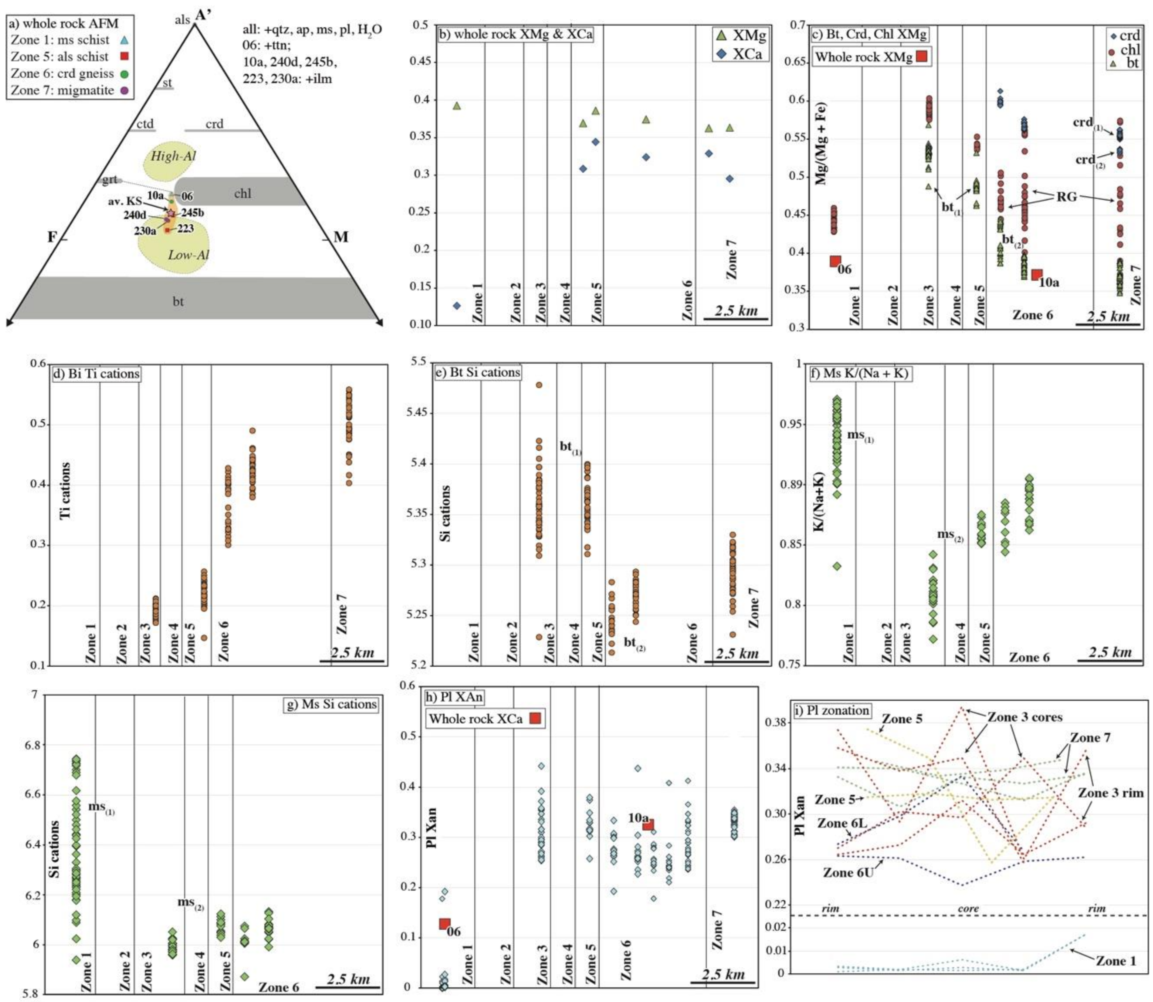

Figure 9. a) AFM diagram showing the plotting positions of whole rock XRF analyses across the Kluane Schist (red starts, Fig. 2). b) Variation in whole rock Mg/(Mg +Fe) (XMg) and Ca/(Ca + Na) (XCa) with petrological zone. c-h) Mineral chemistry *v.* petrological zone across the Kluane Schist (green stars, Fig. 2); in (c and h) we compare mineral chemistry with the bulk composition (red squares) of proximal samples (see Fig. 2). In (c, e, f, g) we highlight distinct populations of

biotite ($bt_{1/2}$), cordierite ($crd_{1/2}$) and muscovite ($ms_{1/2}$) which are outlined further in the main text. i) plagioclase zonation with petrological zone.

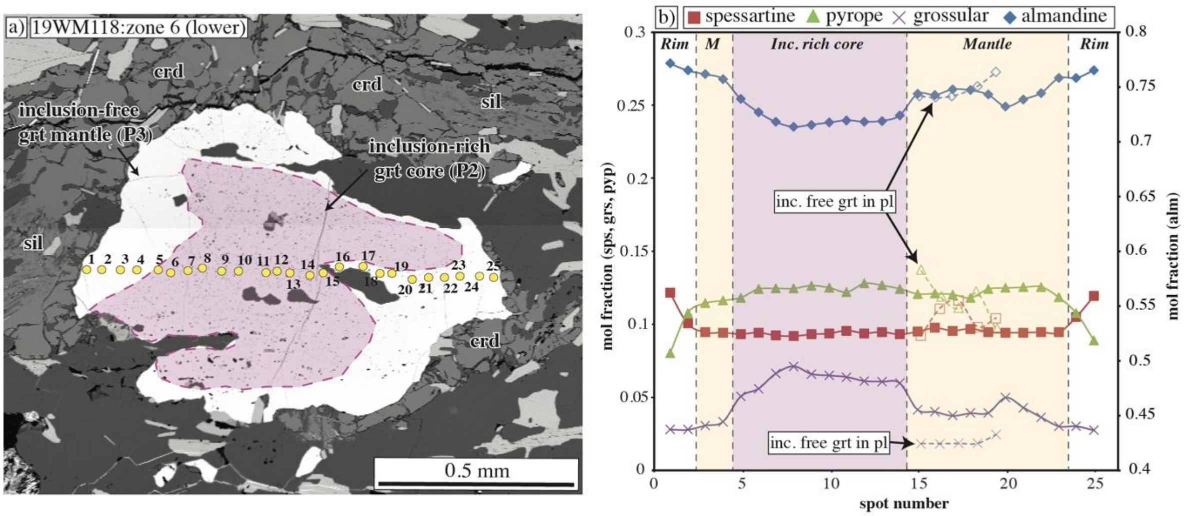

Figure 10. Garnet composition line profile. a) BSE image of a typical of a population (3) inclusion-free garnet mantling a population (2) cloudy core as described in the main text. Yellow spots outline location of probe analyses. b) Rim-to-rim profiles of end-member mole fractions of the garnet shown in (a); end-member mole fractions for a representative fine, inclusion-free garnet typical of zone 5 assemblages (see Fig. 6f) are also superimposed with dashed lines. (inc. free grt in pl = inclusion free garnet in plagioclase).

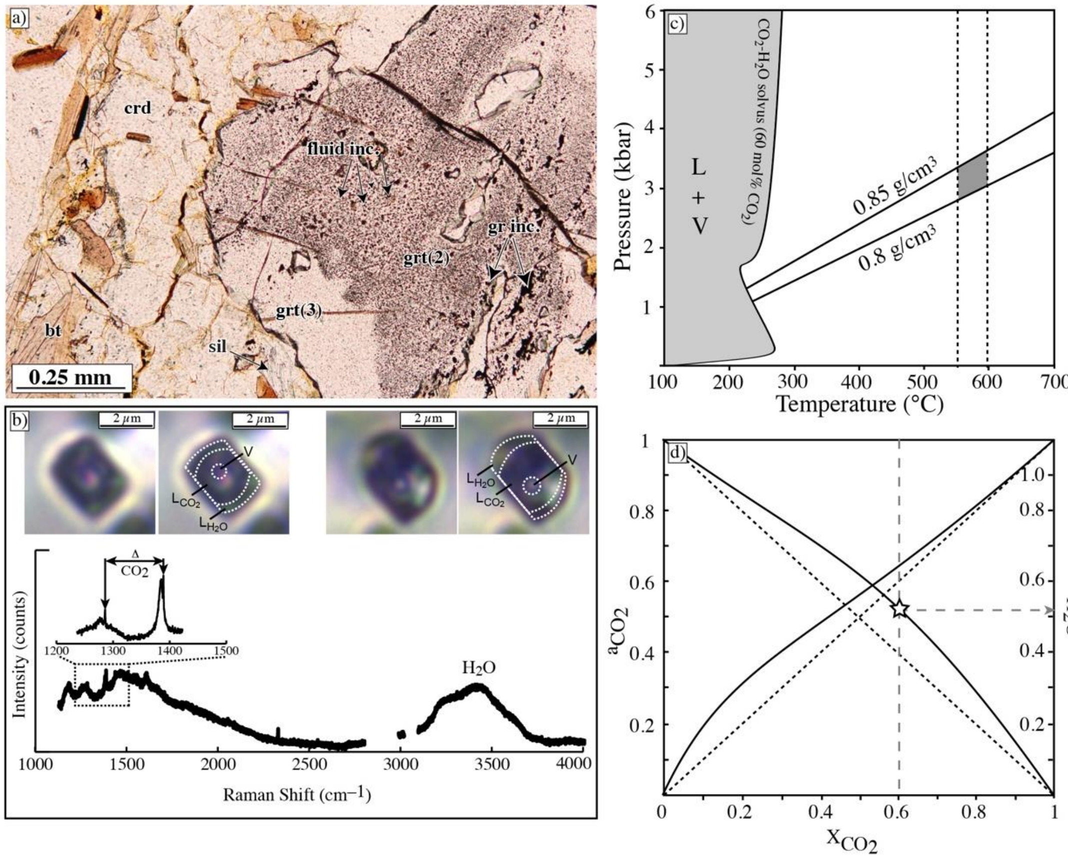

Figure 11. a) Fluid and graphite inclusions within garnet from sample 19WM118. b) Images of example fluid inclusions with their Raman spectrum, highlighting carbonic liquid and vapor. Carbonic liquid (L_{CO2}) occupies the highest proportion at ~80 vol.% with other aqueous liquid (L_{H2O}) ~15 vol.% and the innermost vapor bubble (V) ~5 vol.%. Comparison between these inclusions highlights the consistency in these ratios we observed during analysis. c) Fluid inclusion isochoric model. Maximum pressure of ~3.7 kbar calculated using an estimated total bulk density of 0.8–0.85 g/cm^3 and temperature of 550–600 °C. d) CO_2–H_2O activity-composition relationships of Aranovich and Newton (1999) combined with our results from Raman spectroscopic analysis provide an estimation of $aH_2O = 0.5$.

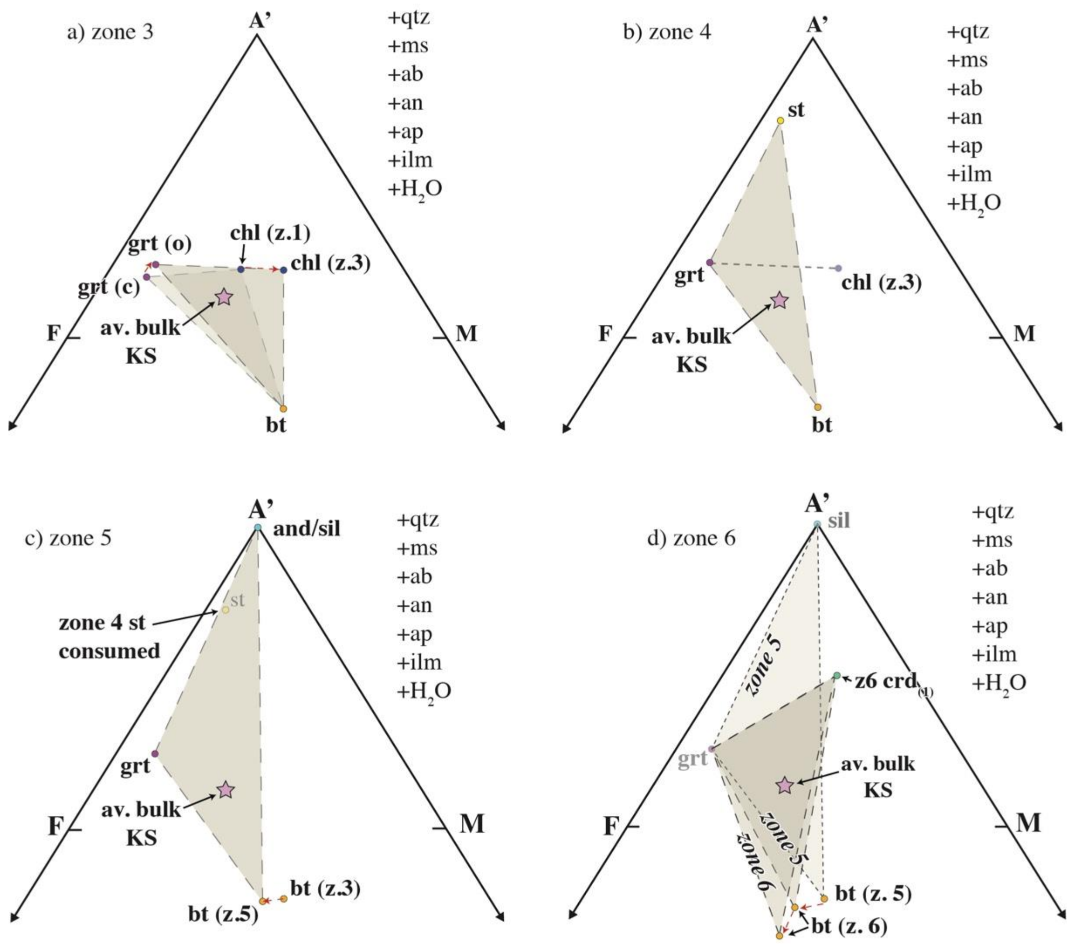

Figure 12. a-d) AFM plots projected from quartz (qtz), muscovite (ms), albite (ab), anorthite (an), apatite (ap), ilmenite (ilm) and fluid (H_2O) highlighting the key phase relationships resulting in the development of petrological zones 3–6. The pink star represents the average bulk composition of the Kluane Schist (see Fig. 9a). Where mineral abbreviations have subscripts these match the petrological zone from which the analysed mineral composition was recovered. In (a) grt(c) and grt(o) refer to the average garnet core and outer domain compositions from a representative zone 3 garnet respectively.

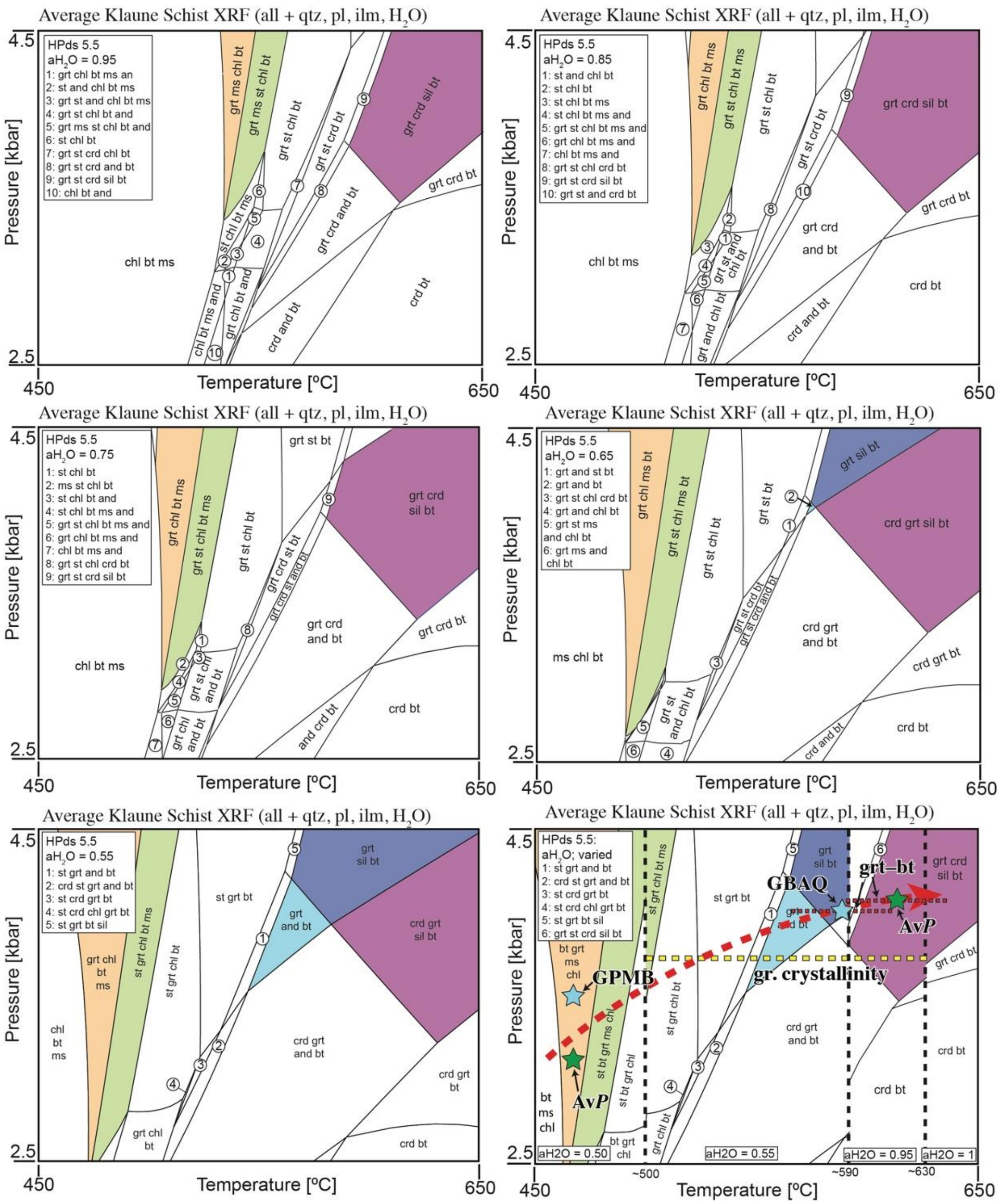

Figure 13. Phase diagrams calculated for an average Kluane Schist bulk composition over a select *P*-*T* area (450–650ºC, 2.5–4.5 kbar) using ds5.5, the activity models described in the main text and a variety of aH2O values. Zone 3 assemblages are highlighted in orange, zone 4 in green, zone 5 in blue and zone 6 in purple. a) aH2O = 0.95, b) aH2O = 0.85 c) aH2O = 0.75, d) aH2O = 0.65, e)

aH$_2$O = 0.55. Across all diagrams we only observe the prediction of the zone 5 assemblage garnet–andalusite–biotite (+ quartz–plagioclase–ilmenite–H$_2$O; light blue) below aH$_2$O values of 0.65. e) A best-fit model accounting for observed natural assemblages across the Kluane Schist and their associated *P-T* estimates (see Table 1). Yellow dashed line shows range of temperatures returned from graphite crystallinity (see Fig. S1).

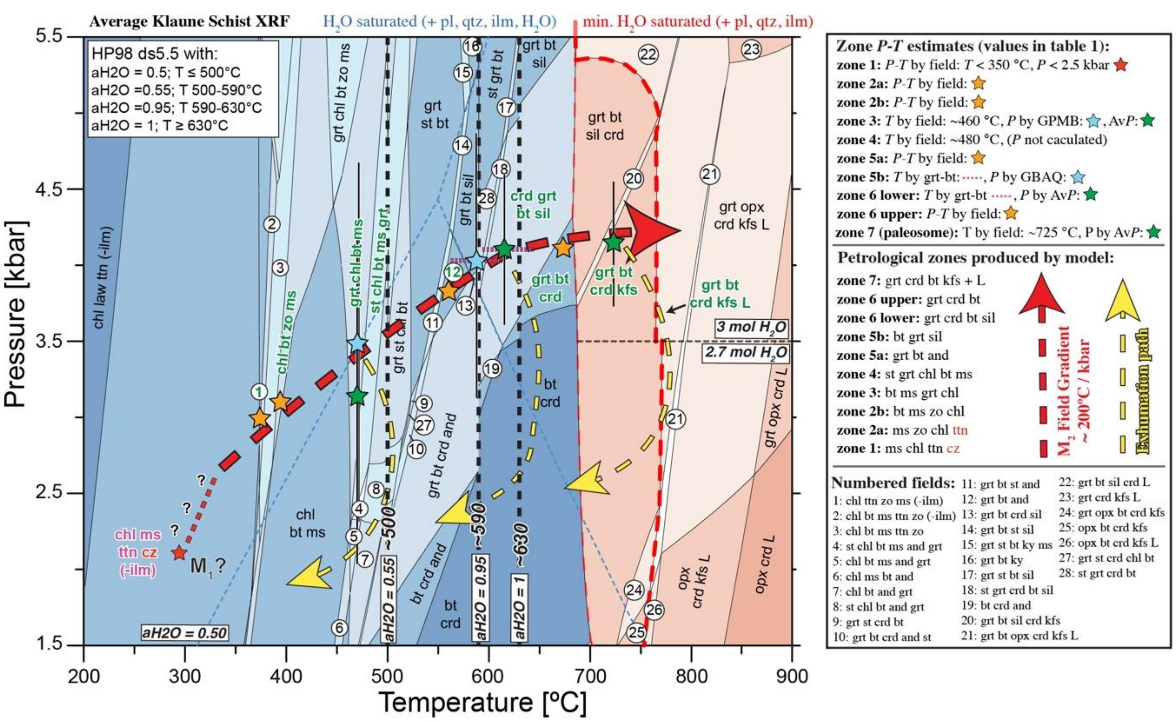

Figure 14. Phase diagram calculated for an average bulk composition of the Kluane Schist using ds5.5 and the activity models described in the main text. Below 500°C aH$_2$O = 0.5, from 500–590°C aH$_2$O = 0.55, from 590–630°C aH$_2$O = 0.95 and above 630°C aH$_2$O = 1 (see Figs. 11, 13 and main text for discussion). Above the wet solidus (thin red dashed line; red shaded fields) models are run with minimally saturated water contents determined at 4.0 and 2.0 kbar (see Fig. S5 and section 3.2). Bold assemblages highlight those best representative of the petrological zones

across the Kluane Schist; pink text highlights zone 1 (M_1) and zones 2-7 (M_2) are highlighted in green. Red text refers to a discrepancy between model prediction and thin section observation (additionally, see text on right); these are discussed further in main text. Conventional barometry estimates are outlined by light blue stars. Av*P* estimates are highlighted by green stars. Pink dashed lines refer to temperature estimates from the garnet-biotite thermometer (Holdaway, 2000). All these *P-T* estimates, along with their 1-sigma uncertainties, can be found in Table 1. Collectively our results suggest the petrological zones across the Kluane Schist are best represented as a set of nested, clockwise *P-T* loops where peak conditions define a metamorphic field gradient of ~200ºC/kbar.

Tables:

TABLE 1. PRESSURE AND TEMPERATURE ESTIMATES ACROSS THE KLUANE SCHIST

Petrologic zone	Zone 3				Zone 5	Zone 6	Zone 7	
Sample	19WM262				19WM120	19WM118	19WM123	
aH_2O	0.3	0.4	0.5	0.6	1.0	1.0	0.4	1.0
Av*P* (kbar)	3.56 ±0.8	3.42 ±0.9	3.12 ±1.1	3.35 ±1.0	*N/A*	4.1± 0.5	4.13 ±0.4	4.43 ±0.6
Conventional barometry (kbar)	*a*H_2O = 1 GPMB: 3.47 ± 1.2				*a*H_2O = 1 GBAQ: 3.94 ± 1.8	*N/A*	*N/A*	
grt–bt temperature (ºC)	*N/A*				*a*H_2O = 1 590 ± 25	*a*H_2O = 1 615 ± 25	*N/A*	

Table 1. Summary of the *P-T* estimates completed across the Kluane Schist (see Fig. 2 for sample locations). Av*P* = average pressure estimate; GPMB = garnet–plagioclase–muscovite–biotite barometer estimate; GBAQ = garnet–biotite–Al-silicate–quartz barometer estimate; grt-bt =

garnet–biotite thermometer estimate. N/A indicates where estimate was not completed (see main text).